| | |
|---|---|
| **Project Title:** | Robust and Spectrally Selective Aerogels for Solar Receivers |
| **Project Period:** | 02/01/19 – 7/31/20 |
| **Project Budget:** | $455,000 |
| **Submission Date:** | 10/29/20 |
| **Recipient:** | University of Michigan |
| **Address:** | 2800 Plymouth Rd.<br>Ann Arbor, MI 48104 |
| **Award Number:** | DE-EE0008526 |

| | |
|---|---|
| **Principal Investigator:** | Andrej Lenert, Assistant Professor of Chemical Engineering<br>Phone: 734-647-4107<br>Email: alenert@umich.edu |
| **Business Contact:** | Colleen L. Vogler, Senior Project Representative<br>Phone: 734-647-2179<br>Email: clv@umich.edu |

| | |
|---|---|
| **Technology Manager:** | Matthew Bauer |
| **Project Officer:** | Christine Bing |
| **Grant Specialist:** | Laura Gonzalez |
| **Contracting Officer:** | Diana Bobo |

**Executive Summary:**

The development of next generation concentrated solar thermal (CST) plants requires solar receivers to reach high temperatures (> 600°C) while minimizing costs. Efficiently generating such high temperatures using a line-focusing collector and an air-stable receiver has the potential to change the current CSP paradigm because it would: (1) result in large improvements in system-level efficiency of line-focusing systems by enabling the use of high-efficiency supercritical CO2 power cycles; (2) decrease the LCOE of line-focusing systems to meet SETO 2030 goals; (3) maintain performance over the lifetime of the CSP plant by avoiding issues related to breakdown of vacuum.

The use of aerogels as transparent insulating materials (TIMs) in solar thermal receivers has the potential to enable such improvements. Specifically, aerogels can be placed in front of a black (or partially selective) high-temperature absorber to allow sunlight to transmit to the absorber but block heat from escaping. These materials can improve the efficiency and simplify the complexity of thermal transport systems by enabling operation at moderate or no vacuum levels. These potential benefits have been explicitly identified by SETO as 'high impact'. The use of mesoporous silica as a TIM has already led to large improvements in solar collection efficiency. Nevertheless, these materials inherently lose structural integrity and the ability to suppress radiation losses at high temperatures.

Here, we address these challenges by leveraging 1-cycle atomic layer deposition of aluminum oxide onto a silica aerogel to form a thermally stable interfacial layer that is transparent to sunlight but broadly absorbs in the mid-infrared. This interfacial absorption results in a two-fold reduction in measured heat losses from an absorber at 700°C and solar thermal efficiency of 81% at 700°C under 60 Suns, based on measurements of heat loss and solar transmittance. Extended-duration heat treatment reveals that the multicomponent aerogel is stable at high temperatures relative to a silica aerogel.

Furthermore, we experimentally demonstrate the concept of using infrared plasmon resonances to selectively enhance the thermal absorption coefficient of TIMs in order to strongly suppress thermal radiative losses at high temperatures. We term this mechanism plasmon-enhanced greenhouse selectivity (*PEGS*). Unlike silica aerogels, where much of the IR absorption is lost at high temperatures, local surface plasmon resonances (LSPRs) in doped oxide nanoparticles overlap a significant portion of the blackbody spectrum and are maintained at high temperatures.

Overall, this work paves the way for next-generation solar thermal energy using thermally robust transparent insulating materials.

## Table of Contents

***Background:*** ..... ***4***

***Project Objectives:*** ..... ***5***

***Project Results and Discussion:*** ..... ***7***

**1. Thermal transport model and target TIM properties** ..... **7**
1.1 Aerogel thermal transport model ..... 7
1.2 PROPS80: Target aerogel properties ..... 11

**2. Measurement setup for temperature-dependent heat losses** ..... **13**
2.1 Calibrating the emissivity of the absorber surface and demonstrating range ..... 13
2.2 Validating the accuracy of the heat loss measurement ..... 14

**3. Silica aerogels** ..... **15**
3.1 Sol-gel synthesis and optimization ..... 15

**4. Plasmonic aerogels** ..... **18**

**5. ALD-coated aerogels** ..... **22**
5.1 ALD process ..... 22
5.2 Coating uniformity ..... 23
5.3 Properties of ALD-coated aerogels ..... 25

**6. High-temperature heat losses and stability** ..... **29**
6.1 Heat loss from ALD-coated aerogels ..... 29
6.2 Thermal stability of ALD-coated aerogels ..... 30

**7. Modeling efficiency and cost of a line-focusing system with aerogels** ..... **31**
7.1 Linear receiver heat transfer model ..... 32
7.2 Cost modeling using SAM ..... 33

***Inventions, Patents, Publications, and Other Results:*** ..... ***36***

***Path Forward:*** ..... ***37***

***References:*** ..... ***38***

## Background:

The development of next-generation concentrated solar thermal (CST) plants requires solar receivers to reach high temperatures (> 600°C) for efficient generation of carbon-neutral electricity or to provide high-temperature industrial process heat.[1] Achieving temperatures above 600°C is desirable for CST plants because it may enable the use of supercritical $CO_2$ power cycles that have higher thermodynamic efficiency than steam cycles.[2] Moreover, up to 53% of industrial process heating requires temperatures over 600°C.[3] Together, these two demands account for over 45% of our current energy use and their fraction is expected to increase based on projections of electrification of the transportation sector.[4–6]

To reach elevated temperatures, CST plants generally rely on solar selective surfaces or significant optical focusing of sunlight (*i.e.*, solar concentration).[7] Selective surfaces are designed to strongly absorb the solar spectrum while emitting weakly in the infrared – thus reducing thermal radiative losses and enabling higher operating temperatures.[8–12] Although there has been significant progress in selective surfaces for moderate-temperature applications (< 600°C), maintaining selectivity at the high temperatures necessary for future CST applications remains challenging. This is mainly due to thermally activated lattice vibrations, which lead to pronounced electron-phonon scattering and spectral broadening.[13,14] Among reports that have measured thermal emittance at or above 650°C, the lowest reported value is approximately 0.25.[15,16] We note that, despite their prevalence in literature, room-temperature measurements have been shown to significantly underestimate the emittance.[17,18] In addition, interdiffusion and oxidation at high temperatures leads to structural degradation and loss of selectivity in selective surfaces.[19] Consequently, the prevailing approach for reaching high temperatures is the use of high solar concentration ratios (> 200). Unfortunately, large heliostat fields and two-axis solar trackers lead to elevated capital costs.[20] High solar concentration configurations also exhibit lower optical focusing efficiencies (< 65% in power tower configurations) compared to single-axis trackers such as parabolic trough collectors that have optical focusing efficiencies on the order of 80%.[21,22]

An alternative to selective surfaces and high solar concentration are transparent insulating materials (TIMs).[23,24] They suppress re-radiation losses by leveraging the greenhouse effect (Fig. 1a). In a suitable TIM-based receiver, sunlight is transmitted to a solar absorber (e.g., surface, particle, cavity), while thermal radiation is forced to undergo many absorption and re-emission events before escaping. The thermal emittance of the solar absorber is not critical when using such a TIM. To accomplish this task, the thermal absorption coefficient has to be large in the spectral range where blackbody radiation peaks. Unfortunately, to date, these absorption coefficients are too low to achieve very high efficiency at 600°C and above. Specifically, high-porosity mesoporous silica (*e.g.*, silica aerogels), which is a leading solar TIM because of its high solar transparency and low thermal conductivity,[25–28] suffers from large radiative losses at high temperatures. These losses are mainly due to desorption of water and dehydroxylation of surface silanol groups at higher temperatures,[29,30] resulting in low absorption below 5 μm. The resulting impact on efficiency is large because ~60% of the blackbody emitted power lies below 5

µm at 700°C.Even at the upper bound of practical aerogel thicknesses, losses through this transmission window persist. Previous work on improving the spectral selectivity of silica aerogels has largely focused on improving solar transmission.[29,31–33] Methods to increase the thermal opacity of silica aerogels have been explored for use as advanced thermal insulation, but no work to date has demonstrated increased infrared attenuation in aerogels while maintaining high solar transmission.[34,35] For example, Kuhn *et al.* used micron-sized titania and alumina particles to scatter thermal radiation,[36] while Lee *et al.* used carbon (a broadband absorber) to increase infrared absorption;[37] however, both modifications resulted in loss of solar transparency.

In addition to becoming less insulating, silica aerogels become less stable at elevated temperatures. Recent work[38] from Evelyn Wang's group (MIT) investigated how extended high temperatures exposure (tens of days) affects the size of silica aerogels and on their solar thermal efficiency. They showed that after annealing aerogels at 400ºC and 600ºC for 50 days, the (footprint) area of aerogel pucks plateaus around a shrinkage of 23% and 33% relative to as-synthesized, respectively. At 800ºC, however, the area of the aerogels does not plateau. After ~150 days, the area of the aerogel decreased ~75%. These results highlight that improved thermal stability of aerogels is required for next-generation CSP applications (>600ºC).

## Project Objectives:

The aim of this project is to develop multicomponent aerogels with high AM1.5D transmittance, high infrared absorption, and low thermal conductivity. To this end, we will incorporate thermally stable oxides to enhance the suppression of radiative heat losses at elevated temperatures and improve the high-temperature stability relative to conventional (silica-only) aerogels. Atomic layer deposition (ALD) will be used to ensure a conformal coating of the porous structure.

The proposed aerogel receiver has the potential to leapfrog the limitations of selective surfaces and conventional aerogels by leveraging thermally robust infrared absorption to suppress outgoing radiation losses. Selective surfaces lose selectivity at high temperatures due to increased parasitic infrared absorption, and in turn emission losses, associated with pronounced lattice vibrations. Meanwhile, conventional (uncoated) silica aerogels suffer from large radiative losses at high temperatures due to dehydroxylation and water desorption, leaving behind a large transmittance window below 5 µm.

Three principal criteria were used to select candidate coating materials: (i) transparent to solar radiation, (ii) stable at elevated temperatures in air, and (iii) have established protocols for atomic layer deposition (ALD). The first two criteria are important for the embodied use of the aerogel as a TIM which is capable of sustaining operation at 700ºC. Furthermore, the PI had prior experience stabilizing micro/nanofabricated thermal emitters for operation at temperatures above 1000ºC using hafnia ALD coatings.[39] Alumina ALD functionalization has also been shown to stabilize a variety of nanostructures, including nanoporous gold structures up to 900ºC.[40]

Similarly, silica aerogels were chosen based on a mixture of criteria: (i) transparent to solar radiation, (ii) suitable infrared absorption due to Si-O-Si vibration, (iii) established protocols for synthesis of aerogels with variable density and pore size. In fact, silica aerogels are the leading TIMs because of their exceptionally high solar transparency.[31]

This SIPS project will systematically investigate the effect of processing parameters on the relevant properties. Experimental characterization of the spectral and thermal properties will be used to inform our heat transfer model and to optimize the processing parameters. Based on our model, we will synthesize optimized multicomponent aerogels and measure receiver efficiency through independent measurements of solar absorption and temperature-dependent heat loss. For example, we aim to demonstrate high AM1.5D absorption (>90%) and low heat losses (<10 kW/m$^2$) with a 700ºC black absorber (using measurements on the same aerogel). These goals are consistent with an overall 80% receiver efficiency where 10% of the incident power is lost in transmission to the absorber and 10% is lost as heat. If, however, one of the properties is worse than our target, the other property will need to be correspondingly better to achieve the overall objective.

The thermal stability of the coated and uncoated aerogels will be evaluated throughout the project by subjecting the aerogels to constant temperature holds at 700ºC of increasing duration. We will investigate ALD of thin layers of a suite of refractory oxides to improve the stability of the aerogel structure at 700ºC.

Lastly, we will model the performance and cost of a scaled-up receiver in a realistic CSP configuration (e.g., parabolic trough collectors (PTC)) to evaluate the potential for further development and commercialization.

We anticipate that achieving the project objectives will: (1) result in large improvements in system-level efficiency of line-focusing systems by enabling the use of high-efficiency supercritical CO2 power cycles; (2) decrease the LCOE of line-focusing systems to meet SETO 2030 goals; (3) maintain performance over the lifetime of the CSP plant by avoiding issues related to breakdown of vacuum. Together, these improvements will facilitate the deployment of cost-effective CSP systems with integrated storage that in turn will accelerate a transition toward reliable solar power.

## Project Results and Discussion:

### 1. Thermal transport model and target TIM properties

The performance of TIM-based receivers depends on the following material properties: solar transmittance, infrared absorption coefficient, and thermal conductivity. In this section, we determine the set of properties required for a TIM to operate with at least 80% efficiency at various temperatures (500 – 700°C) and two different solar concentration ratios (60x and 100x). These results serve as a guide for design of TIMs for next-generation CSP. To define these regions, we use a transport model that iteratively solves the radiative transfer equation (RTE) and the heat transfer equation (HTE). We validated our model through comparison with published models of aerogel-based solar receivers and with measured properties of aerogels synthesized by the project team.

#### 1.1 Aerogel thermal transport model

There are three primary heat fluxes in a TIM-based solar receiver (Figure 1a) – solar radiation in, thermal radiation out, and conduction out. The heat collected by a solar receiver, $Q$, largely depends on the amount of solar radiation transmitted by the TIM to the absorber and the thermal losses to the environment $Q_{loss}$, as shown by the thermal resistance network in Figure 1b. The energy that reaches the absorber directly is given by $\tau C G_s$, where $\tau$ is the solar-weighted transmittance of the TIM, $C$ is the solar concentration ratio, and $G_s$ is the standard AM1.5D incident solar power (1,000 W m$^{-2}$). The absorber is assumed to be a blackbody. Meanwhile, heat losses are a function of the absorber temperature $T_{abs}$ and the thermal resistance of the TIM, which, in turn, depends on its infrared absorption coefficient $\beta$ and the (non-radiative) thermal conductivity $k$. To limit thermal losses, a TIM needs to have a high $\beta$ to suppress radiative losses and a low $k$ to limit conductive losses.

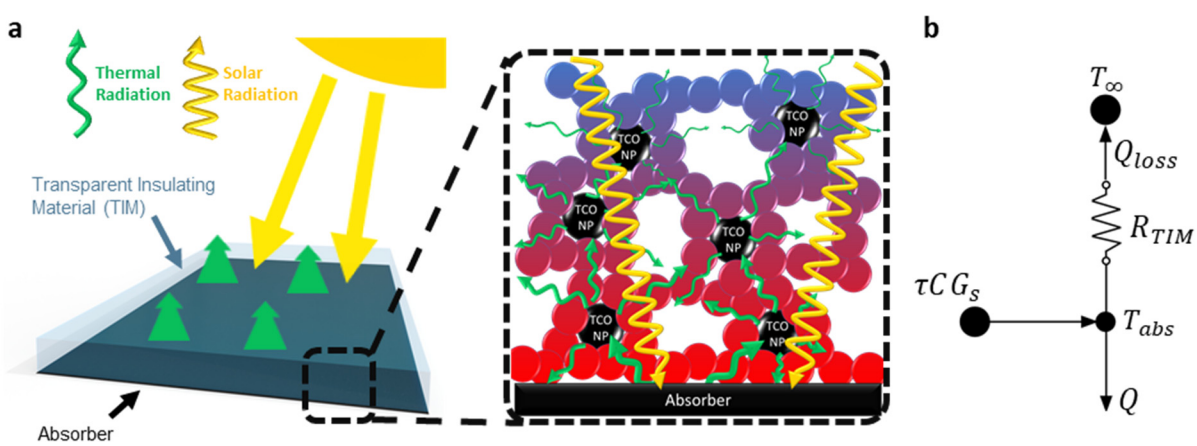


**Figure 1. Solar thermal energy conversion using transparent insulating materials (TIMs). (a) Schematic of a receiver configuration where the TIM is in thermal contact with a blackbody absorbing surface on one side and exposed to the surroundings on the other. Zoomed in schematic shows how absorption inside the TIM can hinder thermal emission. (b) Equivalent thermal resistance diagram approximating transport in a TIM-based solar receiver. The incoming solar radiation ($\tau C G_s$) is either collected ($Q$) or lost to the environment ($Q_{loss}$). Higher thermal resistance ($R_{TIM}$) leads to greater heat collection.**

***RTE-HTE model***

For "good" TIMs, radiation can be dominant heat transfer mechanism at high temperatures. Nevertheless, a model that accounts for both radiation and conduction through the aerogel is necessary to ensure accuracy.

To model thermal transport in TIM-based receiver, we use the continuum heat transfer equation (HTE, Equation 1.1-1.2) in conjunction with the radiative transfer equation (RTE, Equation 1.3).

$$\rho c_v \frac{\partial T}{\partial t} = \nabla \cdot (k \nabla T) + \dot{Q}''' - \nabla \cdot q_r \tag{1.1}$$

$$\nabla \cdot (k \nabla T) - \nabla \cdot q_r = 0 \tag{1.2}$$

The HTE is simplified because we assume steady-state and that the only internal heat generation is due to the divergence of the radiative flux. The analytical 1-dimensional solution to Equation 1.3 is provided in Equation 1.4. The net radiative heat flux, $q_r$, is a sum of the forward propagating (1st and 3rd) and backward propagating (2nd and 4th) terms. Both the HTE and RTE are required because conduction and radiation each play an integral role in the heat transfer through the aerogel. The process starts by first guessing a temperature profile and solving the RTE (Equation 1.4). The solution from the RTE is then used as the $q_r$ term in Equation 1.2. The HTE is solved numerically with the finite difference method and a new temperature profile is produced. This process is iterated until a solution is reached.

$$\frac{dI_\nu}{d\tau} = -I_\nu + (1-\omega) I_\nu + \frac{\omega}{4\pi} \int_0^{4\pi} I_\nu(\boldsymbol{s_i}) \Phi(\boldsymbol{s_i}, \boldsymbol{s}) d\Omega_i \tag{1.3}$$

$$q_r(\tau) = 2J_1 E_3(\tau) - 2J_2 E_3(\tau_L - \tau) + 2\pi \int_0^{\tau} S(\tau') E_2(\tau - \tau') d\tau' - 2\pi \int_{\tau}^{\tau_L} S(\tau') E_2(\tau_L - \tau) d\tau' \tag{1.4}$$

The RTE is computationally expensive to solve because it is an integro-differential equation that is wavelength dependent. To simplify the calculation, we divide the electromagnetic spectrum into approximately 10 bands. Wavelength-dependent parameters are averaged for each band.

For the boundary conditions, the temperature at the TIM/absorber interface is fixed, and a convective boundary condition (U = 20 W $m^{-2}$/K, $T_\infty$ = 295K) is used at the air/TIM interface.

<u>Assumptions</u>:

- One-dimensional transport. I.e. thickness is much smaller than the aerogel width/length.
- Steady-state conditions.
- The (non-radiative) thermal conductivity is assumed to negligibly depend on temperature.

- Attenuation in at wavelengths below 1 um is due to scattering, while the attenuation above 1 um is due to absorption.
- Scattering is isotropic ($\Phi$ in Equation 1.3 is equal to unity), which is consistent with previous work.[41]

Validation:

We validated our model through comparison with published models[27] of aerogel-based solar receivers. Our model was able to match the results in literature[27] when using the same input parameters as that work.

***Scattering and absorption properties***

There are two extinction mechanisms in silica aerogels: absorption and scattering. Aerogels mainly scatter at lower wavelengths (< 1 micron) and absorb at long wavelengths (> 1 micron). For absorption, we used the extinction coefficients from literature.

To predict the scattering of the aerogels below 1 micron, we used a Rayleigh scattering model (Equations 1.5-1.8). The approximations of the model are justified because the size of the silica particles and aerogel pores are much smaller than the wavelengths of visible light. The inputs to the model are the density of the aerogel and the size of the scattering particle/pore. The density of our aerogels is about 200 kg $m^{-3}$, and literature[29] has shown the scattering centers are about 6-8 nm for our synthesis.

The wavelength-dependent size parameter, $x$, is calculated from the radius of the particle/pore (Eq. 1.6). The absorption and scattering efficiencies, $Q_{abs}$ and $Q_{scat}$, are calculated using Equation 1.7. Finally, the relative extinction coefficients, $\beta_{abs}$ and $\beta_{scat}$, are calculated using Equation 1.8.

$$\tilde{n} = n + ik = \sqrt{\epsilon' + i\epsilon''} \quad (1.5)$$

$$x = \frac{2\pi R}{\lambda} \quad (1.6)$$

$$Q_{abs} = 4x * imag\left(\frac{\tilde{n}^2 - 1}{\tilde{n}^2 + 2}\right) \quad (1.7a)$$

$$Q_{scat} = \frac{8}{3}x^4 * abs\left(\frac{\tilde{n}^2 - 1}{\tilde{n}^2 + 2}\right) \quad (1.7b)$$

$$\beta_{abs} = \frac{3}{4} * \frac{Q_{abs}}{R} \quad (1.8a)$$

$$\beta_{scat} = \frac{3}{4} * \frac{Q_{scat}}{R} \quad (1.8b)$$

Validation:

**Outcome**: < 20% error in 6/10 bands. In partial fulfillment of milestone #1d.

| # | Month of completion | Performance Metric | Success Value | Assessment Tool / Method of Measuring Success Value | Verification Process | Metric Justification, Additional Notes |
|---|---|---|---|---|---|---|
| **1d**<br><br>task: 1.3 | 12 | RTE model validation | < 20% error (within each wavelength band) | **Maximum.** Model output compared to UV-VIS-NIR, FTIR, hot disk. 10 wavelength bands between 0.3-8 microns. | Data and report sent to DOE. Synthesized analytical data | <20% error on a wavelength basis is considered excellent agreement for solid-state materials. |

The results from our modeling are compared to experimental measurements on aerogels synthesized by the project team in Figure 2.

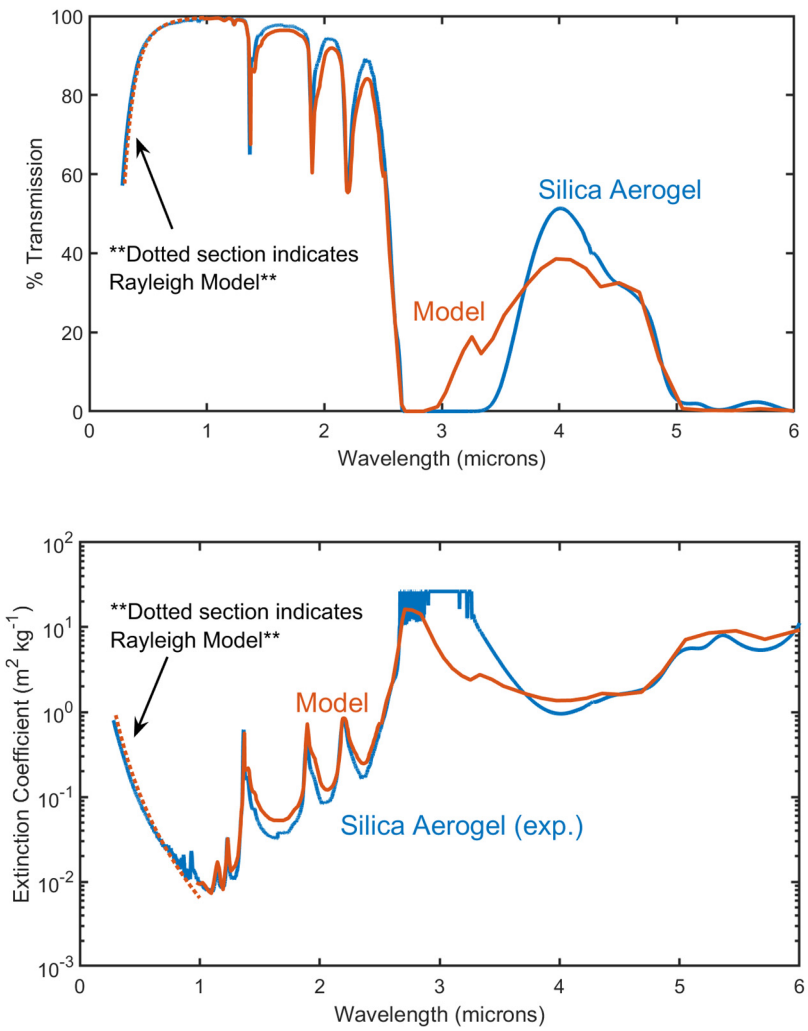


**Figure 2. Comparison of modeled and measured spectral properties of aerogels.**

The model generally agrees with our experimental results. Discrepancies (Table 1) in the transmission of the aerogels are primarily due to water content which can vary considerably depending on the synthesis steps and environment. Nevertheless, we were able to accurately predict the blackbody averaged extinction accurately.

**Table 1. Difference between relative extinction for measured and modeled values**

| Band (microns) | Measured (rel.) | Model prediction (rel.) | Error (%) |
|---|---|---|---|
| 0.3 - 0.5 | 0.252 | 0.277 | 9.91 |
| 0.5 - 0.7 | 0.0487 | 0.0455 | 6.62 |
| 0.7 - 1.0 | 0.0176 | 0.0134 | 23.5 |
| 1.0 - 1.4 | 0.0492 | 0.0591 | 20.0 |
| 1.4 - 1.8 | 0.0487 | 0.0751 | 54.3 |
| 1.8 - 2.2 | 0.189 | 0.243 | 28.4 |
| 2.2 - 3.0 | 9.29 | 5.73 | 38.4 |
| 3.0 - 4.0 | 9.54 | 2.29 | 76.0 |
| 4.0 - 5.0 | 1.87 | 2.11 | 12.9 |
| 5.0 - 8.0 | 12.5 | 14.2 | 13.4 |

## 1.2 PROPS80: Target aerogel properties

**Outcome**: Identified PROPS80 regions at various temperature including at 700ºC and 100 Suns. In fulfillment of milestone #1a.

| | | | | | | |
|---|---|---|---|---|---|---|
| **1a**<br><br>task: 1.1 | 3 | Predicted receiver efficiency | > 80% at 700C and 100x Solar Concentration Ratio (*i.e. 100 suns)*. | **Sensitivity analysis**. RTE-HTE model will be validated and used to identify combinations of PROPertieS that allow the 80% efficiency metric to be met (PROPS80). | Report sent to DOE for verification. Agree upon acceptable combinations of performance metrics.<br><br>Graphical Output(s) indicating parameter space of interest | The success value was chosen based on initial performance modeling. Enables high system-level efficiency for line focusing systems at 700 C. |

The efficiency of a TIM-based receiver is defined by Equation 1.9:

$$\eta = \frac{Q}{CG_s} \tag{1.9}$$

where $Q$ is the heat collected, $G_s$ is the nominal solar irradiance (AM1.5D), and $C$ is the solar concentration ratio.

Given an absorber temperature and a solar concentration ratio, the combination of the three parameters ($\tau$, $\beta$, and $k$) that enable 80% efficiency for a 5 mm thick TIM were calculated. The results are presented in Figure 3. The shaded regions indicate combinations of the parameters with >80% receiver efficiency. We will refer to this parametric space as PROPS80. The boundary of each shaded region designates 80% efficiency, while any point away from the boundary and toward the upper right has a higher efficiency. PROPS80 regions increase with decreasing absorber temperature (largest for 500°C). The regions also increase with increasing concentration ratio (larger for 100x than 60x).

To put these PROPS80 regions in context, the state-of-the-art silica aerogels are approximately characterized by $\tau$ of 0.90-0.97, $k$ of 20-30 mW m$^{-1}$K$^{-1}$, and a $\beta$ of ~5 cm$^{-1}$ (at RT, 1 bar).[29,42] These silica aerogels are within the PROPS80 region (>80% efficiency) only at relatively low temperatures and high concentrations such as 500°C and $C$ = 100 (shown for reference on figure 2a).

This parametric study shows that suppressing thermal losses, by selectively increasing $\beta$, is a promising route for achieving 80% efficiency at temperatures characteristic of next-gen CSP. Alternate routes are also viable, such as decreasing thermal conductivity and increasing solar transmittance. However, prior aerogel work has focused extensively on these two properties, while increasing $\beta$ has not been investigated to the same extent.

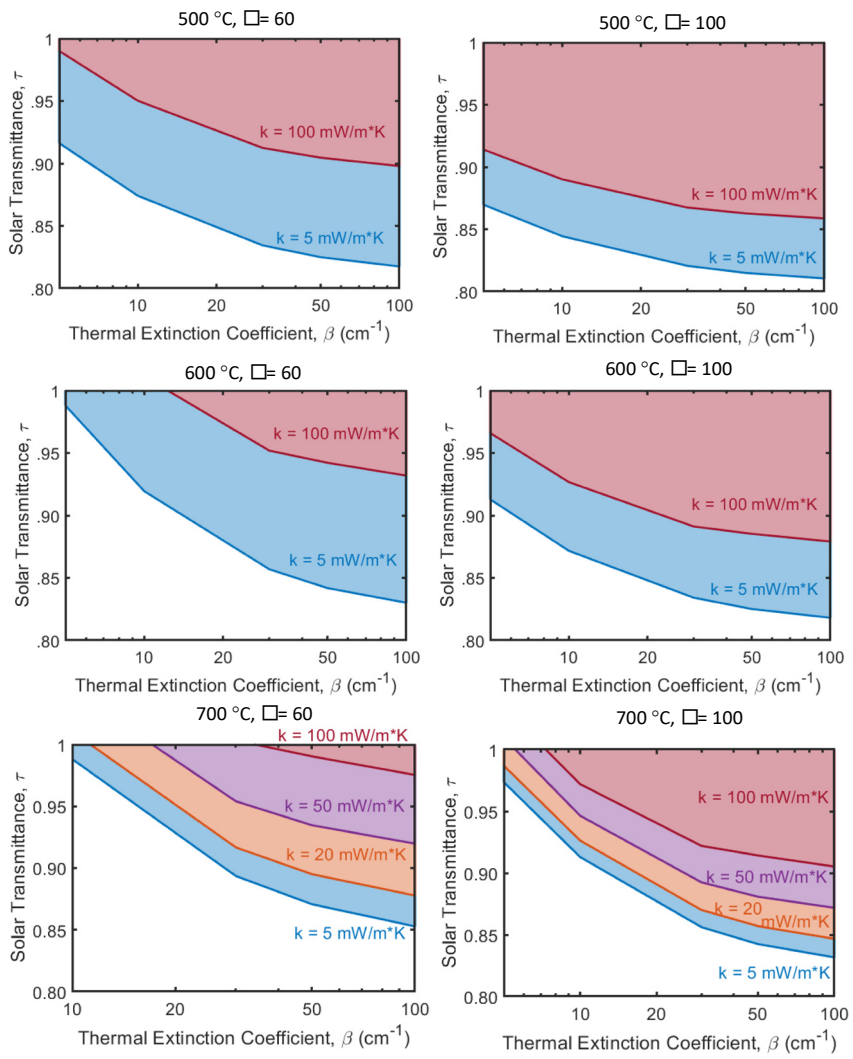


**Figure 3. TIM properties required for >80% receiver efficiency with absorber temperatures ranging from 500 to 700°C and concentration ratios ranging from 60 to 100 suns.**

## 2. Measurement setup for temperature-dependent heat losses

**Outcome**: Developed heat loss measurement technique with <5% error and a temperature range up to 700ºC. In fulfillment of milestone #1b.

| | | | | | | |
|---|---|---|---|---|---|---|
| **1b**<br><br>task: 1.2 | 6 | Heat loss measurement accuracy and temp. range | Accuracy: within 10%<br><br>Range: 25-700C | **Student's t-test.** Measurement compared to hot disk. At least 10 measurements on each sample using each technique. (Average, 90% CI) | Data and report sent to DOE.<br><br>Data Format: conductivity (W/mK), and heat loss (W/m$^2$) vs. temperature<br><br>Error propagation of experiment | 10% error is standard for thermal conductivity measurements (laser flash, etc.) |

We have developed a lab-scale experimental platform that allows us to apply a constant temperature boundary condition to an absorber surface and to measure the heat flowing through and out of the aerogel (Figure 4). A high-temperature stage (*Instec Inc.*) is used to control the absorber temperature from 25 to 700ºC. A heat flux sensor (XP 26 9C, greenTEG AG) is grounded to a cold plate (copper) maintained near room temperature using a forced air stream. The surface of the sensor is covered with an adhesive reference blackbody surface (Metal Velvet, Acktar).

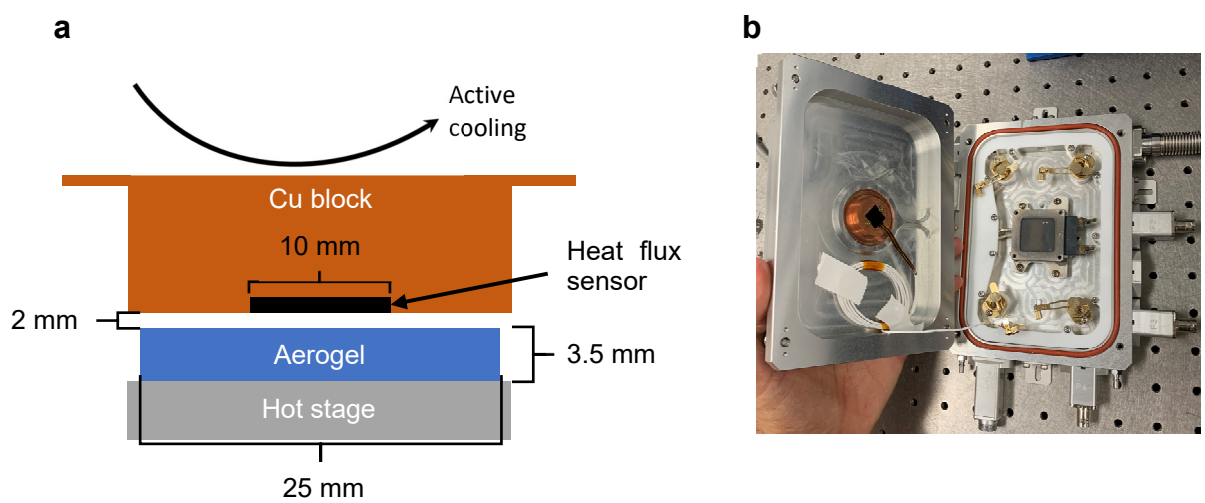


**Figure 4. Heat loss measurement setup: (a) schematic and (b) photo.**

### 2.1 Calibrating the emissivity of the absorber surface and demonstrating range

Figure 5 shows the heat flux versus the temperature of the hot stage. This demonstrates the capability of our system to reach 700ºC. The samples are held at each temperature for 30 minutes to allow the system to equilibrate. Between holds, the ramp rate is 10°C/min. Temperature ramp up and ramp downs are conducted to ensure no hysteresis.

By measuring heat flux as a function of temperature without the aerogel, we can determine the surface emissivity of the hot stage (i.e., absorber surface). Knowing this

emissivity allows us to make comparisons to our aerogel model and ensure that the experiments and the models are consistent. This validated model can then be used to predict heat losses when the aerogel is paired with another absorber surface, such as a blackbody or selective surface.

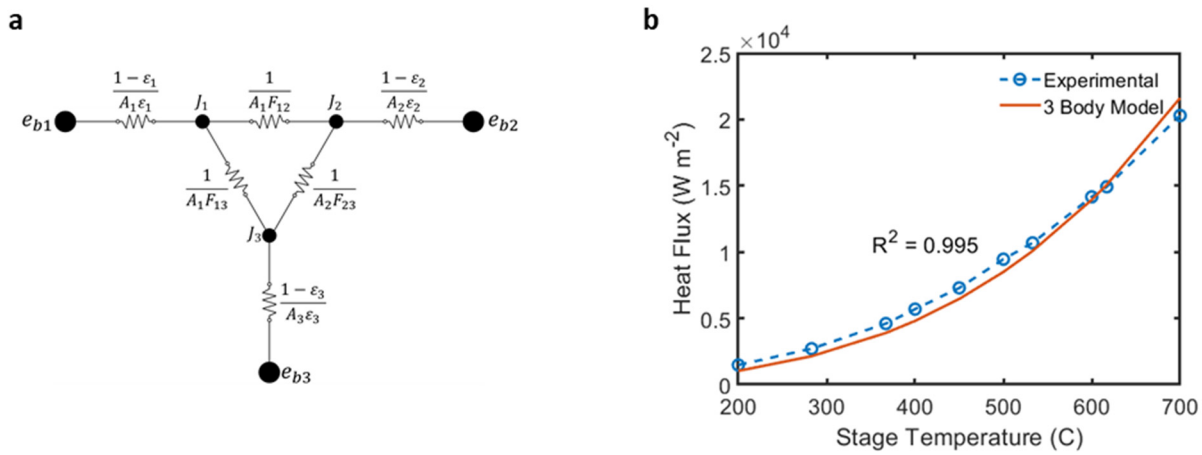


**Figure 5. Stage surface emissivity and temperature range. (a) The radiative heat transfer from the aerogel/emitter to the heat flux sensor is modeled using a 3-body diffuse radiative network. The resistances include the emissivity of the surfaces and the view factors. (b) Fitting the experimental data to the 3-body model gives a surface emissivity of ~0.55.**

The thermal emissivity of the hot-stage surface was determined by conducting a calibration measurement without an aerogel sample. A three-body radiative transfer network was used to account for the finite view factor between the heat flux sensor and the hot-stage surface (Figure 5). The three bodies are labelled as follows: hot stage (1), heat flux sensor (2), surroundings (3). In the model, $e_b$ is the emissive power of the surface, $A$ is the area, $F_{ij}$ is the view factor from surface $i$ to surface $j$, $\varepsilon$ is the surface emissivity, and $J$ is the surface radiosity. The emissivity of the heat flux sensor covered in blackbody tape is 0.98, as determined by an FT-IR measurement. Our fit to the experimental data produced a hot-stage emissivity of 0.55 ± 0.02 (Figure S7b).

***Important note about uncertainty***: Uncertainty in all experimental quantities, including the hot-stage emissivity, were evaluated based on propagation of the following errors: variance (using a t-distribution with a 95% confidence interval), instrument error and resolution error. All errors were assumed to be uncorrelated.

## 2.2 Validating the accuracy of the heat loss measurement

To validate the heat loss measurement (Figure 6), we compared the measured thermal conductivity of polystyrene foam to the transient plane source. The transient plane source method was implemented using a commercial instrument (TPS, HotDisk) equipped with a thin spiral-resistor source/sensor (5465, HotDisk). The raw conductivities determined by the software were corrected using a polynomial correlation proposed by Zheng *et al*[43] for highly insulating samples.

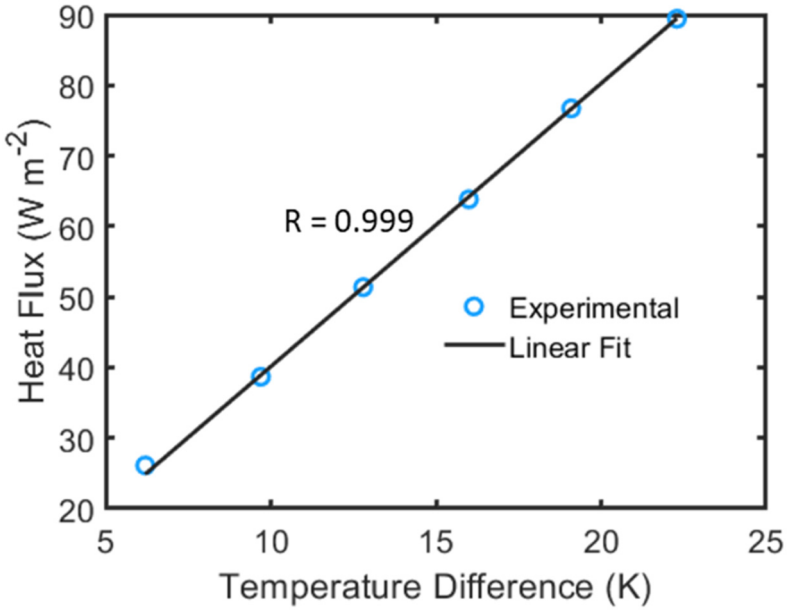


**Figure 6. Hot stage validation. Thermal conductivity of polystyrene foam insulation measured using the hot stage setup.**

The hot stage measurement is performed by setting the temperature of the stage and measuring the steady-state heat flux, and the temperature of the cold sensor. We performed this experiment at different hot stage temperatures. The measured heat flux as a function of the temperature difference between the hot and cold side is shown in Figure 5. The heat flux scales linearly with the temperature difference according to the thermal conductivity of the sample. These data allow us to report a thermal conductivity of 48.5 +/- 14.1 mW/m/K. The reported uncertainty accounts for the uncertainty associated with the thermocouple measurement, the heat flux measurement, the geometry, and the linear regression (via the method of sampling with replacement). The value measured by the hot stage setup agrees (within the uncertainty) with the value determined using the commercial TPS measurement of 49.6 +/- 2.3 mW/m/K. The TPS measurement was repeated 10 times. The uncertainty calculation is described in 2.1.

## 3. Silica aerogels

### 3.1 Sol-gel synthesis and optimization

We conducted a 3 x 3 parametric study varying the aging time and the pH of the catalyst solution. We tested three different aging times ranging from 1 to 3 weeks. We also altered the pH by increasing the concentration of ammonia in solution relative to our baseline recipe (1x, 2x, 4x). Each batch consisted of at least 4 aerogel samples (approximately 1 inch in diameter and 3 mm in thickness).

Aerogels were synthesized *via* a sol-gel polymerization of tetramethylorthosilicate (TMOS, 218472, Sigma-Aldrich) with DI water and ammonia ($NH_3$, 341428, 2.0M in methanol, Sigma-Aldrich) as the catalyst. We first prepared two solutions. TMOS is

diluted in methanol (MeOH, 322415, Sigma-Aldrich), and ammonia solution is added to DI water. The two solutions are then mixed in plastic syringes where gelation is allowed to proceed. Once the wet gels formed, they were aged with daily ethanol washes to remove contaminants and water. The aerogels were then dried using $CO_2$ critical point drying (CPD, model 915B, Tousimis). Upon drying, the aerogels were annealed at 400°C for 24 hours in a Vulcan oven to remove any organic contaminants or surfactants.

The results from the parametric study show that increasing the amount of catalyst and the aging time increases the transmittance at low wavelengths (less than 1 micron). This region is dominated by scattering from voids/pores and the solid framework (i.e. particles). Increasing the amount of catalyst in the formation of silica aerogels promotes the hydrolysis reaction which leads to increased crosslinking. The increased crosslinking results in smaller silica particles and smaller voids - therefore decreasing scattering. Increased aging time has a similar effect on the structure as increasing the catalyst loading and hence, reduces scattering.

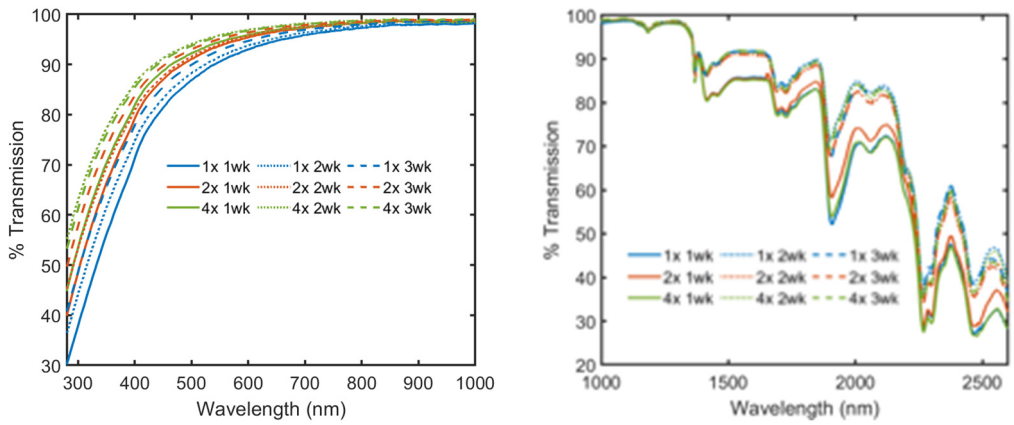


**Figure 7. Effects of synthesis parameters on transmittance of aerogels**

**Table 2. Parametric effects on solar weighted transmittance**

| Catalyst | Aged 1 week | Aged 2 weeks | Aged 3 weeks |
|---|---|---|---|
| 1x | 90.2 | 91.8 | 92.7 |
| 2x | 92.4 | 91.3 | 94.0 |
| 4x | 92.7 | 94.6 | 94.5 |

As for the infrared region of the solar spectrum (1 to 2 microns), it appears that the amount of catalyst has an insignificant effect on the scattering. On the other hand, increasing aging time increases the transmittance in this region because ethanol pulls water out of the aerogel. Hence, increased aging results in a lower water content and thus, less infrared absorption. It is important to note, however, that water evolves from the aerogels

when they are heated to high temperatures. Therefore, we would expect that the effect of aging/pH on infrared transmission to be negligible when used at elevated temperatures (>400ºC), such as those in solar thermal applications.

The parametric study shows that there is a trend in thermal conductivity with increasing aging time. Increasing aging time *decreases* conductivity with 2/3 samples. This trend can be explained by the decreasing water content within aerogels with aging. Since water accounts for a large fraction of the mass and can provide a conduction path, lower water content can decrease thermal conductivity. On the other hand, increasing the amount of catalyst tends to *increase* conductivity. As stated previously, increasing the amount of catalyst increases crosslinking and reduces the average pore size. Thus, increased catalyst could have a two-fold effect: (i) more paths for heat transfer via the aerogel backbone due to greater crosslinking, (ii) the size of the particles is smaller which restricts heat flow. Further investigation into these competing mechanisms and their relative importance at elevated temperatures may be warranted.

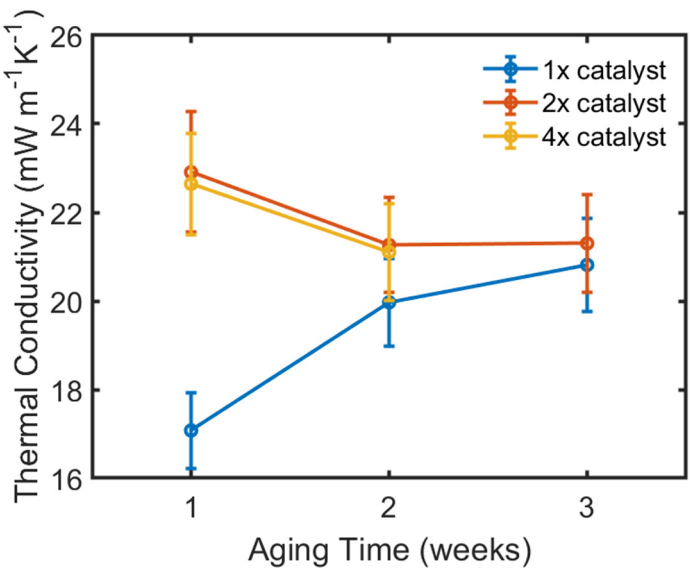


**Figure 8. Effects of aging and catalyst loading on thermal conductivity**

## 4. Plasmonic aerogels

In this section, we discuss our recent demonstration (OSTI# 1673748)[44] on the use of infrared plasmon resonances to selectively enhance the thermal absorption coefficient of TIMs, in order to strongly suppress thermal radiative losses at high temperatures. We term this mechanism plasmon-enhanced greenhouse selectivity (*PEGS*). Unlike silica aerogels, where much of the IR absorption is lost at high temperatures, local surface plasmon resonances (LSPRs) in doped oxide nanoparticles overlap a significant portion of the blackbody spectrum and are maintained at high temperatures. Within the aerogel transparency window (< 5 μm), our plasmonic aerogel has significantly higher absorption than state-of-the-art silica aerogels.[31]

To experimentally demonstrate the proposed *PEGS* mechanism, we synthesized plasmonic aerogels (PAs) by incorporating indium tin oxide (ITO) NPs into a silica aerogel (Figure 9). Drops of disbursed ITO NPs in ethanol (US7656, US Research Nanomaterials, Inc) were added to the water-ammonia solution before mixing. The NPs have an average diameter of 18 nm and are incorporated in solution before gelation and drying. The resulting aerogels are 3.5 mm thick with varying volume fractions of NPs (up to 0.024%). The addition of the NPs has a negligible effect on the density and thermal conductivity of the aerogels which are approximately 160 kg $m^{-3}$ and ~20 mW/m/K, respectively. The ITO NPs have an LSPR at approximately 5 microns (Figure 9). Notably, the highest volume fraction of TCO NPs eliminates the undesirable mid-IR transparency window. By adding the measured extinction coefficient of the ITO NPs to literature silica aerogel extinction coefficients,[42] we estimate that $\beta$ increases from 7.2 to 18.2 $cm^{-1}$ at 700°C.

The measured solar weighted transmittance decreases from 0.95 (without NPs) to 0.70 at the highest volume fraction. Aggregation of ITO NPs is largely responsible for this observed decrease in $\tau$. ITO NPs concentrated in an ethanol suspension were obtained from US Research Nanomaterials. Figure 10 shows measured the scattering and absorption properties by UV-Vis-NIR and Fourier transform infrared (FTIR). For the former, we measured the transmittance of the particles in a diluted solution. The results show that the particles have low attenuation throughout most of the solar spectrum but absorb in the infrared. We also determined the scattering properties of the ITO NPs by fitting a Rayleigh scattering model to the extinction coefficient at short wavelengths. The slope of the Rayleigh prediction agrees with the data between 300-450 nm, consistent with the spherical geometry of the ITO NPs and the particle size (~18 nm), which is smaller than the wavelength of interest. Using the Rayleigh model, we simulate the expected transmission of the ITO NPs in a silica aerogel matrix (Figure 10). The experimental transmission spectra are lower than predicted by simulation, likely due to aggregation of ITO NPs during synthesis, resulting in effectively larger particles that produce scattering at longer wavelengths. NP aggregation is also observed in the TEM images of the ITO NPs in the silica matrix. In particular, some of the ITO NPs are aggregated without being encapsulated by the aerogel matrix.

The observed aggregation can likely be avoided with further optimization of the synthesis procedure. Nevertheless, the increase in infrared absorption from the ITO NPs outweighs the decrease in solar transmittance, resulting in higher $\Gamma$. In the radiative limit,

our models show that the addition of plasmonic nanoparticles increases the greenhouse selectivity of the aerogel from 2.3 to 4.5 which translates to an increase in $T_{max}$ from 506°C to 661°C under 10 suns (Figure 9). We note that this calculation assumes negligible conduction and that the radiative properties of the aerogel and NPs are independent of temperature.

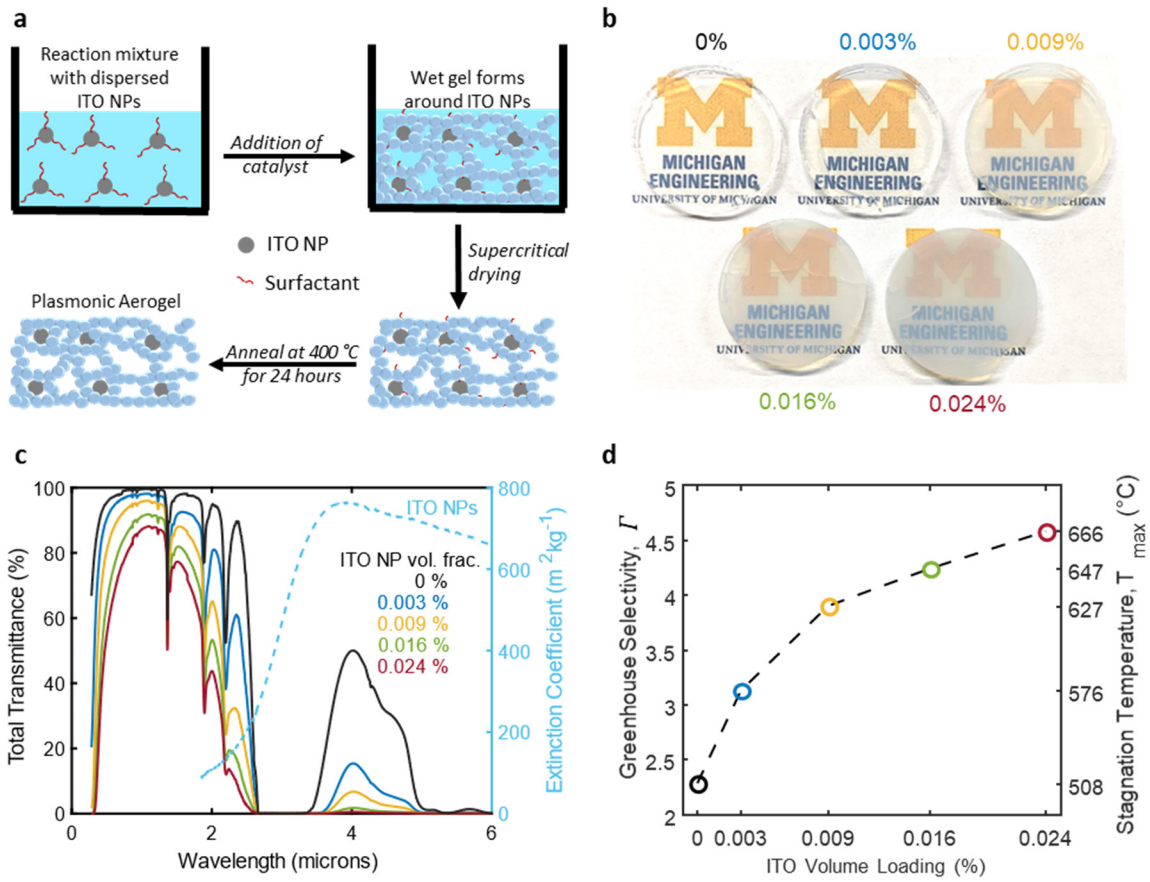


**Figure 9. Radiative properties of synthesized plasmonic aerogels.[45] (a) Process of fabricating plasmonic aerogels (PAs): ITO NPs are mixed into the aerogel reaction mixture; upon addition of the sol-gel catalyst, the aerogel backbone forms around the particles; critical point drying and annealing removes the surfactant. (b) Photograph of the plasmonic aerogels. (c) Measured total transmittance of the PAs (solid lines) and infrared absorption of the ITO NPs (dotted line). The presence of the ITO increases the infrared absorption by eliminating the infrared transparency window of silica aerogels. The peak of the ITO absorption aligns well with the infrared transparency window of silica aerogels. (d) Greenhouse selectivity of the PAs at their stagnation temperature at 10 Suns. The increase in greenhouse selectivity enables higher temperatures.**

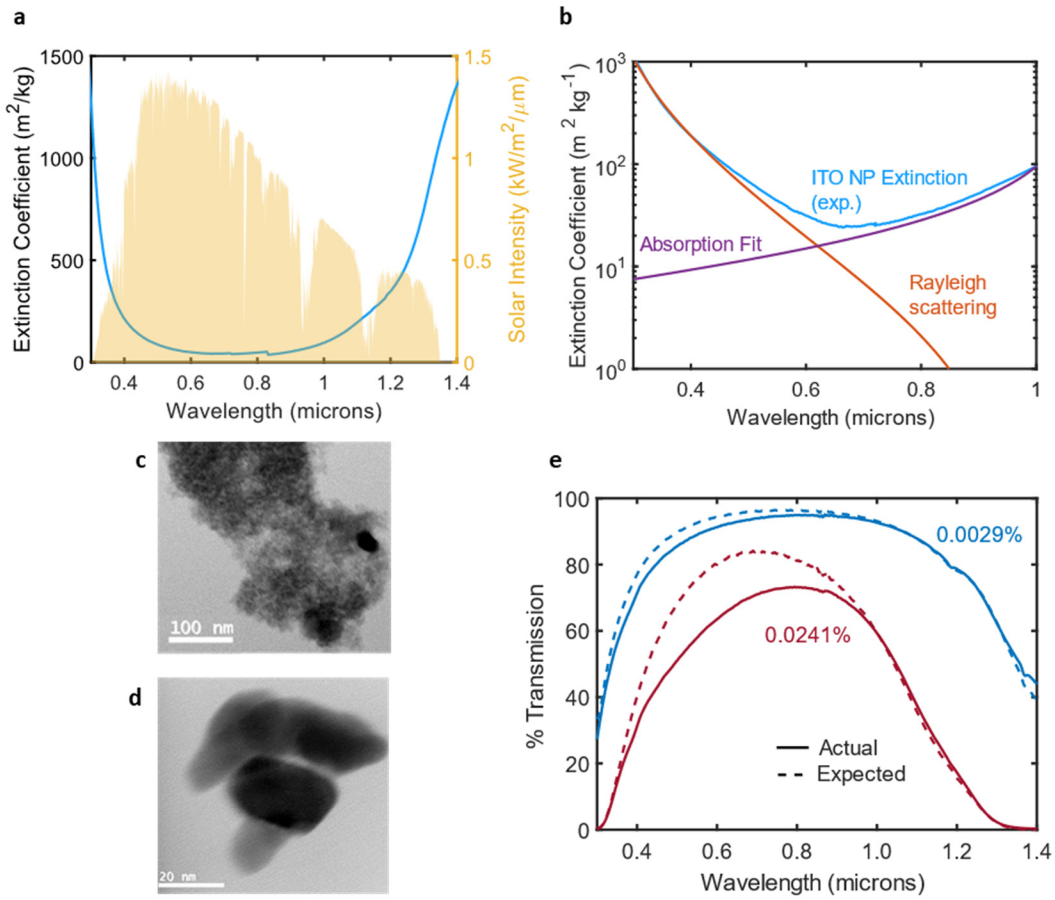


**Figure 10. Scattering and absorption properties of the ITO NPs. (a) UV-Vis spectra of the ITO NPs dispersed in ethanol. (b) Rayleigh scattering model agrees with measured extinction at short wavelengths. The remaining extinction is attributed to absorption. (c) Transmission spectra of unannealed plasmonic aerogels showing lower transmission than predicted by the Rayleigh model, likely due to increased scattering resulting from NP aggregation. (d) TEM images of ITO NPs (0.024% by volume) in silica aerogel showing evidence of aggregation.**

To experimentally determine the effective greenhouse selectivity of the PAs, which accounts for conduction through the solid phase and the temperature-dependence of the thermal absorption coefficient, we measure the heat flux through the aerogels (*i.e.*, heat loss) using the calorimetric setup shown in Figure 11. The aerogels are placed between a variable-temperature hot stage and a heat flux sensor that is grounded to cold plate maintained at ~30°C and covered by a reference blackbody surface. Figure 11 shows how the measured heat flux increases with hot-stage temperature. We note that the aerogel samples were stable at 700°C for the duration of the experiment.

Figure 11c shows the reduction in heat losses with increasing ITO volume fraction. Notably, a nearly 50% reduction in heat losses (at 700°C) is observed for the highest ITO volume loading relative to the silica aerogel. The decrease in the heat flux is attributed to the plasmon-enhanced suppression of radiative transfer resulting from the increased infrared absorption and consequently decreased mean free path of thermal radiation.

These measurements provide validation that radiative losses are indeed significant at elevated temperatures in our PAs and can be significantly suppressed *via PEGS*. Furthermore, the experimental data shows good agreement with our numerical heat transfer model which rigorously combines the radiative transfer equation with the heat transfer equation.

We report the effective greenhouse selectivity ($\Gamma_{eff}$) using the measured heat losses and solar-weighted transmittances. The greenhouse selectivity increases from 2.2 to 3.5 with increasing ITO volume loading. We note that while the 0.024% sample produces the highest stagnation temperature (largest $\Gamma_{eff}$), it may not be the optimal volume fraction once a performance or cost optimization of the entire CST system is considered. Nevertheless, these experimental measurements demonstrate that *PEGS* is strong enough to overcome parasitic conduction in evacuated aerogels. We further confirm the strength of the *PEGS* mechanism by modeling the heat losses through the aerogel at ambient pressure where conduction is ~20 mW/m/K compared to ~8 mW/m/K in vacuum. Even at ambient pressure, the *PEGS* mechanism is strong enough to overcome conductive losses.

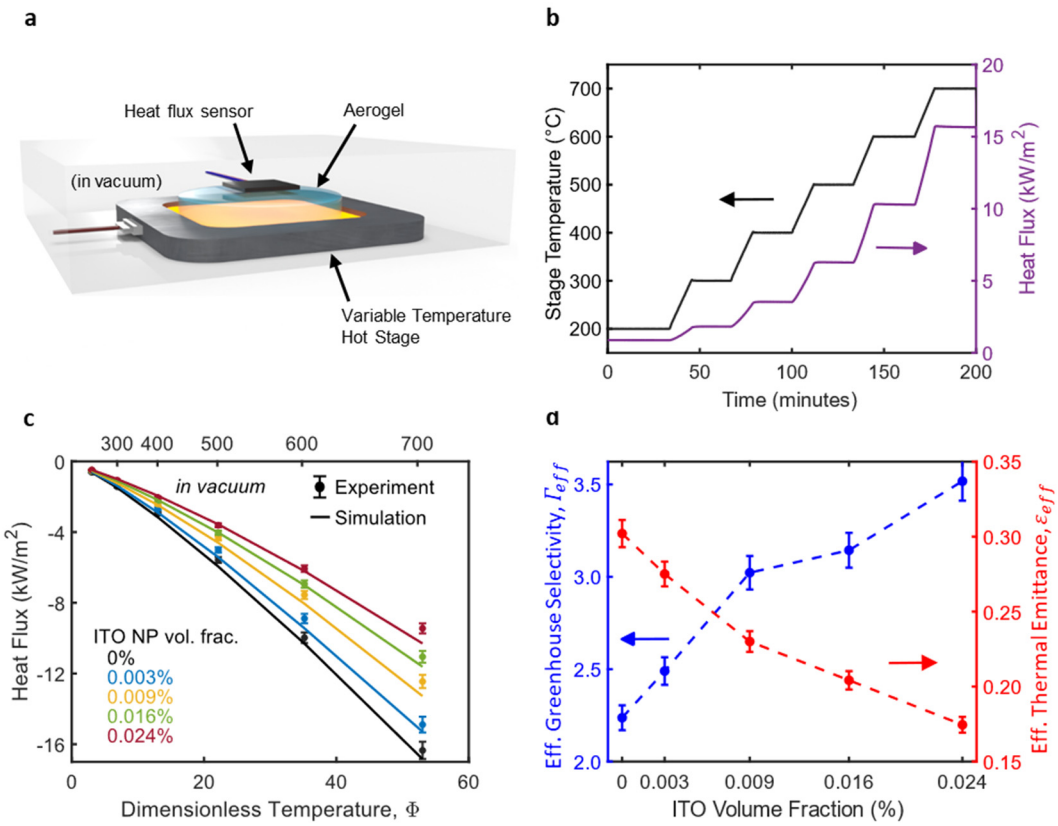


**Figure 11. Experimental demonstration of PEGS. (a) The experimental setup used to measure the heat flux through the PAs under dark, vacuum conditions. A heat flux sensor with blackbody tape measures heat loss from the aerogel *versus* varying absorber surface temperature. (b) Example time-series data of the measured heat flux *versus* the stage temperature setpoint. (c) Experimental (points) and simulated (solid lines) temperature-**

**dependent heat losses with increasing ITO loading. (d) Effective greenhouse selectivity (blue) and thermal emittance (red) of the PAs at 700 ºC.**

Lastly, we compare the performance of PAs to reported selective surfaces based on effective thermal emittance ($\varepsilon_{eff}$) calculated using measured heat losses according to Eq. 2. Figure 11d shows $\varepsilon_{eff}$ at 700°C as a function of ITO fraction. For the aerogel without NPs, which is representative of the state-of-the-art, $\varepsilon_{eff}$ is 0.30 ± 0.02 at 700ºC. In contrast, the addition of ITO NPs decreases $\varepsilon_{eff}$ to 0.17 ± 0.01.[16,46,47]

Our work thus demonstrates that the *PEGS* mechanism is strong enough to significantly suppress thermal losses and increase the greenhouse selectivity of TIM-based solar thermal receivers. More broadly, we show that plasmonic resonances can be used to tune the spectral selectivity of mesoporous media, such as silica aerogels.

## 5. ALD-coated aerogels

### 5.1 ALD process

This section discusses the main steps in our ALD process and how we have developed a recipe for coating of thick aerogels (>3 mm). This demonstrates the power of ALD in coating ultra-high aspect ratios (>10,000:1 based on the aerogel pore size), which would be very difficult to accomplish via any other technique.

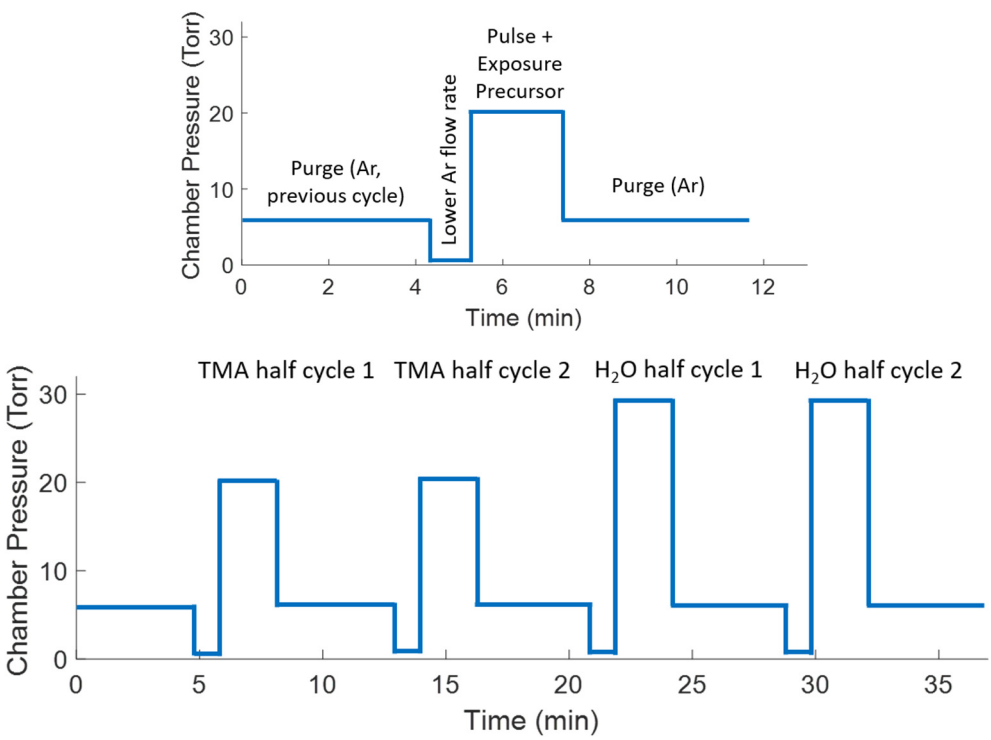


**Figure 12. Schematic of the sequence of steps during ALD, a) one half cycle and b) one cycle consisting of two half cycles of trimethylaluminum (TMA) and two half cycles of deionized water.**

The ALD recipe (Figure 12) was tuned to increase precursor penetration into the aerogel and provide a large enough precursor dose to sufficiently coat the aerogel. After an initial purge for one hour to remove any adsorbates from the aerogel surface, 5 deionized water precycles were performed to ensure sufficient hydroxyl groups on the surface of the aerogel, followed by 1 ALD cycle. A cycle consisted of a series of half cycles for precursor A, followed by a series of half cycles of precursor B. One precursor half cycle involves the following steps: after the purge step in the previous half cycle, Ar flow is decreased from 70 sccm to 10 sccm to lower the absolute pressure in the chamber. This allows for a greater pressure difference when the precursor is pulsed, both allowing for more precursor to be pulsed into the chamber in less time, and improving diffusion into the aerogel. The ALD chamber is isolated from the pump and the precursor is pulsed. The aerogel is exposed to the precursor for a certain time period, during an "exposure" step. An Ar purge, generally double the exposure time, at 70 sccm is then performed to help remove any reaction products, remaining precursor, and air that has leaked in that could result in non-ideal ALD growth. The product molecules ($CH_4$) and important air components ($H_2O$, $O_2$) have higher diffusion coefficients than TMA, so this purge time should be sufficient. This half cycle is repeated a number of times before exposing the aerogel to the counter reactant, in order to provide sufficient precursor to maximize aerogel coating.

## 5.2 Coating uniformity

**Outcome**: < 9% variation in concentration within aerogel. In fulfillment of milestone #1c.

| | | | | | | |
|---|---|---|---|---|---|---|
| **1c**<br><br>task: 2.2 | 12 | Uniform concentration of ALD coating | < 20 % variation in concentration (by volume) within each aerogel | **Maximum.** Measured using EDS cross-sectional mapping (Average, 90% CI). At least 10 pts collected on each aerogel (uniform sampling). At least 2 aerogels (3 mm thick). | Report sent to DOE. Synthesized analytical data | 20% variation can be tolerated based on preliminary modeling |

In order to uniformly coat the aerogels using ALD, the amount of precursor and exposure time were varied. An example of a uniform coating using 1 cycle of 60 pulses of ~20 Torr TMA, followed by 60 pulses of ~30 Torr of water is shown below in Figure 13. This sample demonstrated a variation in atomic percentage of 8.9% through the cross section according to energy-dispersive x-ray spectroscopy (EDAX) measurements. Multiple scans on each sample showed similar atomic percentages and variations.

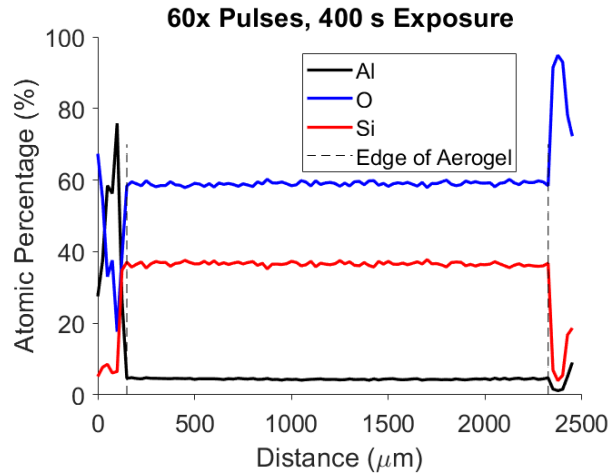


**Figure 13. Uniform ALD along aerogel cross-section, as measured by EDAX**

Uniform coating of aerogels was a key challenge that we needed to overcome. We based our initial recipes on published literature but these attempts were unsuccessful at conformally coating our aerogels. To overcome this barrier and uniformly coat the aerogels using ALD, we designed a systematic sweep of ALD parameters (Figure 14). The amount of precursor and exposure time were varied. A summary of the effects of exposure time and number of pulses is shown below, following a design of experiments where number of precursor pulses and exposure time are varied. In all cases, 1 cycle of ALD $Al_2O_3$ is performed, and the precursor purge time is set at double the exposure time. In order to allow for easier interpretation, the Al/Si ratio is averaged over 5 equal lengths along the aerogel cross section. Below a threshold of ~45 pulses, the atomic percentage of Al relative to Si is relatively low. This ratio appears to asymptote between 45 and 60 pulses, suggesting saturated coverage, a critical aspect of ALD. The uniformity also appears to improve with exposure time, demonstrated by a flattening of the Al/Si ratio through the cross section. This may be due to improved penetration into the nanopores closer to the center of the aerogel. It is also possible that some variation in the Al/Si ratio is due to density variations within the bare $SiO_2$ aerogel. This possible density variation will be investigated using X-ray tomography.

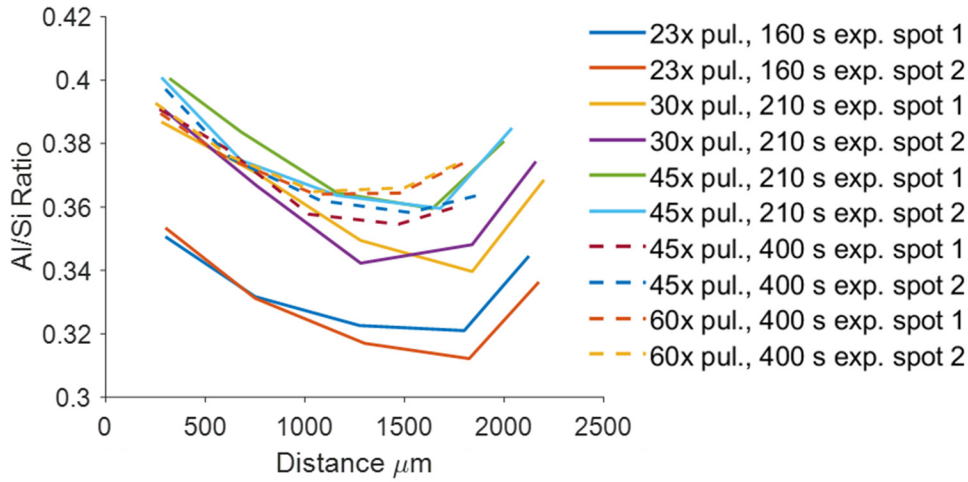


**Figure 14. Effects of ALD process parameters on coating uniformity**

Our laboratory-scale ALD process is performed in a batch reactor. This is consistent with commercial ALD batch reactors, for example chambers designed by Applied Materials and used by Intel can simultaneously coat hundreds of wafers at a time by ALD. However, for commercial purposes, we are not limited to batch processing. The Dasgupta group at UM has built a "spatial ALD" instrument, compatible with continuous processing and roll-to-roll manufacturing.

Using our current reactor, to fully coat one a monolithic aerogel (25 mm diameter by 3 mm depth) with 1 cycle of alumina, takes ~30 hours. However, the coating process is not optimized, and it may be possible to cut down the coating time to ~10-20 hours in our lab reactor. Decreasing the coating time is largely limited by the diffusion of the ALD precursors into the aerogel, as well as the precursor dose we can safely input into our reactor at one time. To project commercial processing times, we have developed a model to determine the ALD coating time for monolithic aerogels. In industrial applications, using significantly higher precursor doses and partial pressures (~380 Torr for trimethylaluminum and deionized water), it should be possible to coat similar monolithic aerogels in less than 15 minutes.

## 5.3 Properties of ALD-coated aerogels

**Outcome**: 92.2 (±0.01) % solar weighted transmittance, 36 (±0.02) mW/m/K thermal conductivity and 27.1 1/cm absorption coefficient. In fulfillment of milestones #2a-c.

| | | | | | | |
|---|---|---|---|---|---|---|
| **2a**<br><br>tasks: 2.1-2.3 | 12 | Solar (AM1.5D) transmittance | > PROPS80 criteria<br>(same samples as 2b,c) | **Student's t-test.** Measured using UV-Vis- NIR. At least 10 measurements on each sample (Average, 90% CI). At least 2 aerogels. | Data and report sent to DOE.<br>Data format: spectral total transmittance (% vs. wavelength) | Allowable: 10% loss of transmission. Consistent with 80% overall. Remainder of loss due to heat loss. |
| **2b** | 12 | Thermal conductivity | ≤ PROPS80 criteria | **Student's t-test.** Measured using hot disk. At least 10 | Data and report sent to DOE. Data format: W/mK | Allowable: 10% of incident as heat loss. Consistent |

| | | | | | | |
|---|---|---|---|---|---|---|
| tasks: 2.1-2.3 | | (near room-temperature) | (same samples as 2a,c) | measurements on each sample (Average, 90% CI). At least 2 aerogels. | | with 80% overall. Remainder due to transmission loss.<br>Note. Data will be extrapolated to 700 C via physical model |
| **2c**<br>tasks: 2.1-2.3 | 12 | Infrared absorption coefficient | > PROPS80 criteria (same samples as 2a,b) | **Student's t-test**. Measured using UV-VIS-NIR and FTIR. Weighted by 700 C spectrum. At least 5 measurements on each sample (Average, 90% CI). At least 1 aerogel. | Data and report sent to DOE. Data format: spectral absorption coefficient (1/cm vs. wavelength). | Allowable: 10% of incident as heat loss. Consistent with 80% overall. Remainder due to transmission loss.<br>Note: data will be synthesized for interpretation from 500°C-800°C |

Using a modified ALD exposure mode recipe, a conformal and uniform ultrathin alumina coating (~1-2 Å, 1 ALD cycle) was deposited on monolithic silica aerogel pucks, with diameters of ~25 mm and thicknesses of ~3 mm. The uncoated silica aerogels have a water-free density of ~160 kg/m$^3$ while the coated aerogels have a density of ~200 kg/m$^3$. The uncoated and coated aerogels were both found to be amorphous by X-ray diffractometry.

The solar and infrared transmission through the aerogels was measured using ultraviolet-visible-near infrared spectroscopy (UV-Vis-NIR) and Fourier-transform infrared spectroscopy (FTIR). The solar weighted transmittance $\tau$ of the uncoated aerogels was found to be ~96%, while the coated aerogel exhibited a marginal decrease in $\tau$ to ~92% (Figure 15). This is enabled by the aerogel backbone, silica, and the conformal coating, alumina, both being highly transparent in visible and near-IR wavelengths. Hemispherical reflectance data suggests the decrease in $\tau$ is a result of increased scattering at shorter wavelengths (< 1 μm) and increased absorption in the near-infrared.

Although the solar transmission is mildly affected by the ALD alumina coating, the mid-infrared transmission is significantly decreased. Notably, the silica aerogel transparency window (3 – 5 μm) is eliminated in the coated samples, within the sensitivity of the FTIR spectrophotometer. To elucidate the magnitude of the absorption, the extinction coefficients of the uncoated and coated aerogels were measured using KBr FTIR spectroscopy (Figure 15). Because alumina and silica do not absorb in this transparency window, other possible compounds in the coated samples were investigated. Enhanced IR absorption is maintained after annealing at 700°C. Unreacted methyl groups from the ALD deposition process, which uses trimethylaluminum as one of the precursors, may also be present in the coated aerogels after deposition. According to literature IR measurements of methyl groups in silica sol-gels, enhanced absorption is expected from 3.3 – 3.6 μm and 6.5-7.5 μm (Lenza 2001), which is not observed in the samples (Fig. 2b). Methyl groups would also likely be removed during high temperature characterization process. With unreacted methyl groups and excess adsorbed water ruled out as possible causes for increased IR absorption, we hypothesize that at the silica-

alumina interface, a new tertiary phase is formed, sharing some characteristics with aluminosilicate phases.

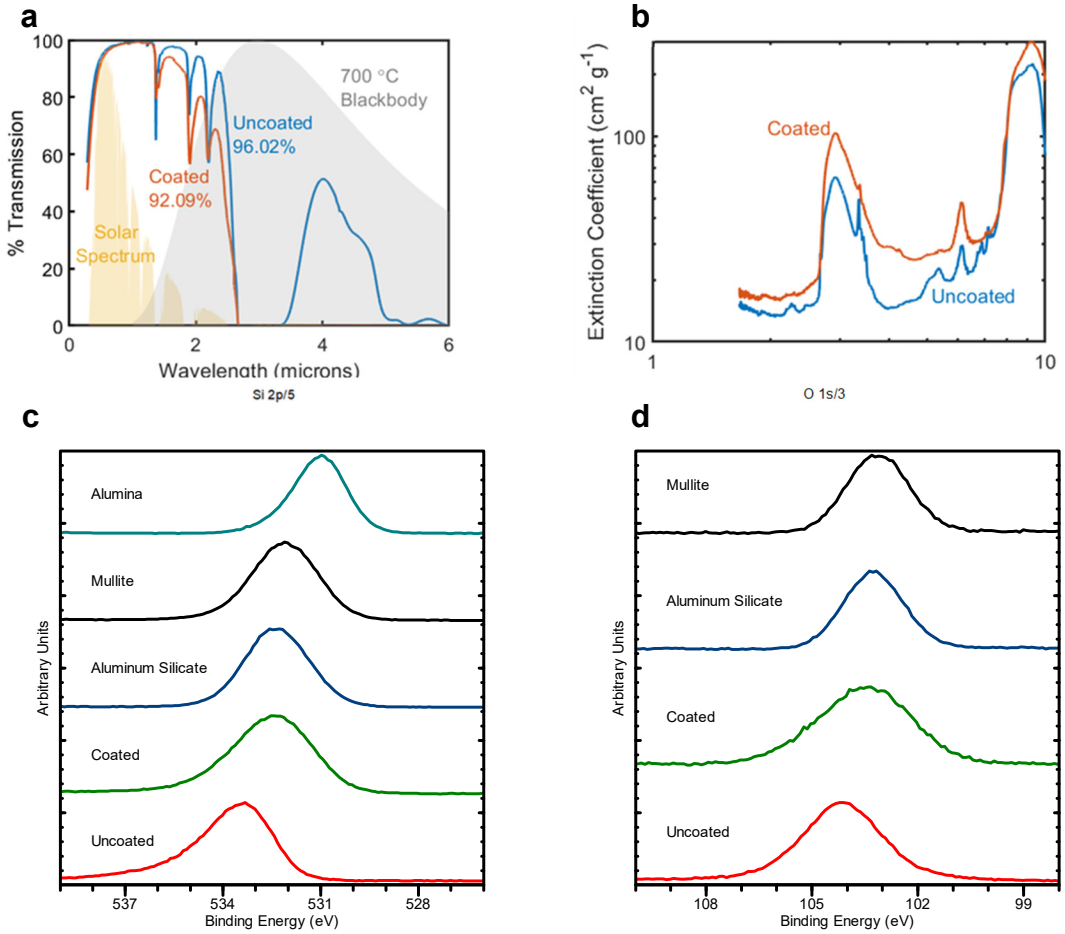


**Figure 15. Properties of uncoated and alumina-coated aerogels. (a) The infrared transparency window of silica aerogels is eliminated in the coated sample, while only decreasing solar-weighted transparency by 4%. (b) The absorption coefficient of the coated aerogel within the transparency window of silica aerogels is higher than uncoated aerogels. (c,d) XPS Si 2p and O 1s cores scans showing that the alumina coating may create an amorphous mullite-like phase.**

It has been previously shown that crystalline-phase mullite, an aluminosilicate, demonstrates enhanced absorption at wavelengths greater than ~4 μm, possibly due to nanometer-scale amorphous silica-rich inclusions.[48] It is possible that a similar structure – a thin aluminosilicate shell around an amorphous silica core – leads to similar enhancements in infrared absorption in the coated sample. However, both the uncoated and coated aerogels are amorphous rather than crystalline, making comparisons to crystalline mullite references in literature convoluted. Although the majority of mullite characterization in literature has been performed on the crystalline phase, there is some evidence that an amorphous mullite-like phase could lead to broadband infrared absorption.[49] Shinohara et al. synthesized stoichiometric mullite from tetraethyl

orthosilicate and boehmite using a sol-gel method, followed by a post anneal to make crystalline mullite. Just below the mullite crystallization temperature, the primarily amorphous gel showed little to no transmittance at wavelengths from 2.8 μm to beyond 5.5 μm. A similar broadband decrease in transmittance is apparent over the same region when comparing coated samples to uncoated aerogels. This suggests that an amorphous mullite-like phase may be present in the coated aerogels at the silica-alumina interface, leading to enhanced infrared absorption in the silica transparency window.

In order to further probe the chemistry of the interfacial layer, X-ray photoelectron spectroscopy (XPS) was used to determine the change in Si and O binding environments after depositing the ALD coating. In each sample, binding energy levels are calibrated to adventitious surface carbon. The ALD coating shifts the Si 2p peak to lower binding energies (Figure 15c), consistent with literature values for expected shifts with increasing aluminum content in aluminosilicate compounds.[50] This was experimentally confirmed using comparisons to mullite and aluminum silicate references, which showed lower Si 2p binding energies compared to uncoated aerogels. Similar binding energy shifts were observed in the O 1s core scans of ALD-coated aerogels (Figure 15d), consistent with literature reports of increasing aluminum content in aluminosilicates.[50] The O 1s peak shifts follow similar trends to experimentally measured aluminosilicate standards, while remaining significantly higher in binding energy than bulk ALD alumina.

Lastly, we measured the thermal conductivity of the uncoated and multicomponent aerogels using the TPS hot disk technique. As expected, the thermal conductivity of the aerogels increased slightly due to the ALD coating. This is a reasonable increase because the mass increase from the coating is about 20%.

Figure 16 and Table 3 below summarize the relevant properties of the ALD coated aerogels and compares them to the properties of the state-of-the-art (SoA) aerogels published in literature. Based on the three important material properties, the coated aerogels are capable of surpassing 80% efficiency at 700 C and 100 Suns, while the SoA aerogels are not.

**Table 3. Summary of key properties of ALD-coated aerogels (at RT, 1 bar)**

| | Solar Weighted Transmittance (%) | Weighted Absorption Coefficient ($cm^{-1}$) | Thermal Conductivity (mW/m/K) |
|---|---|---|---|
| Uncoated | 96.0 | 19.9 | 17.1 ± 0.9 |
| Coated | 92.2 | 27.1 | 22.3 ± 1.1 |

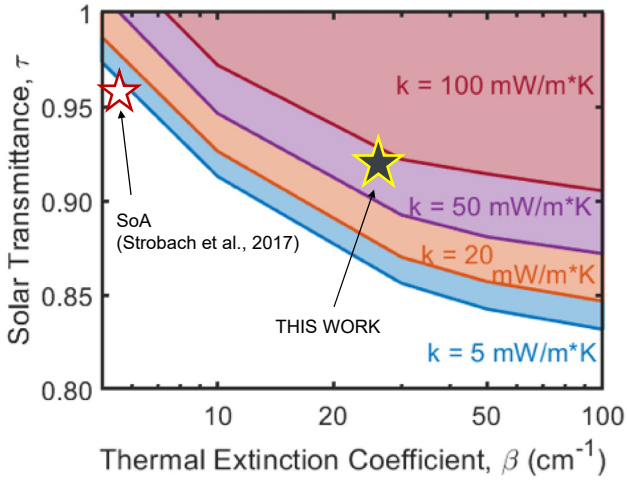


**Figure 16. Properties of coated aerogels (this work) relative to best reported aerogels**

## 6. High-temperature heat losses and stability

Based on the optical and thermal characterization near room temperature described in the previous section, ALD-coated aerogels were selected as the most promising near-term approach for further evaluation at high temperatures. This section describes the evaluation of ALD-coated aerogels in terms of heat loss, receiver efficiency, and thermal stability.

### 6.1 Heat loss from ALD-coated aerogels

**Outcome**. >80% efficiency based on 92% solar transmittance and 7 kW/m$^2$ heat loss at 700ºC. 2 coated aerogels measured. In partial fulfillment of 3a, 3b, EOP-A.

| | | | | | | |
|---|---|---|---|---|---|---|
| **3a**<br><br>tasks: 3.1-3.3 | 15 | Heat loss at 700 C (black absorber) | <10 kW/m$^2$<br><br>(or PROPS80) | **Student's t-test**. At least 10 measurements on each aerogel using heat loss calorimetry (Average, 90% CI). At least 3 aerogels. | Data and report sent to DOE. Data format: heat loss (W/m$^2$) vs. absorber temperature. | The success value was chosen based on initial performance modeling; Allowable: 10% of incident as heat loss. Consistent with 80% overall. Remainder of loss due to heat loss. |
| **3b**<br><br>tasks: 3.1-3.3 | 15 | Solar absorption (near room-temperature, black absorber) | > 90%<br><br>(or PROPS80) | **Student's t-test**. At least 10 measurements on each aerogel using simulated AM1.5 spectrum and calorimetry (Average, 90% CI). At least 3 aerogels. | Data and report sent to DOE. Data format: solar absorption (%). | The success value was chosen based on initial performance modeling; Allowable: 10% loss of transmission. Consistent with 80% overall. Remainder of loss due to heat loss. |
| EOP-A | 18 | Receiver efficiency at 700C and 100x | >80% efficiency | **Student t-test.** Measured using solar absorption and heat loss calorimetry. At least 10 measurements on each aerogel | Data and report sent to DOE for verification. Data format: solar absorption (absorbed power/incident power | The success value was chosen based on initial performance modeling. Enables high system-level efficiency for line |

| | | | | | | |
|---|---|---|---|---|---|---|
| | | | | (Average, 90% CI). At least 3 aerogels. | %), heat loss (W/m$^2$ at 700 C). | focusing systems at 700 C. |

To experimentally demonstrate the improvement in performance, we measure the heat flux through the aerogels at various temperatures in vacuum (Figure 17). The results show the increased infrared absorption of the ALD interfacial layer suppresses heat losses over two-fold compared to the uncoated aerogel. However, it is possible the increased absorption is a result of contaminants from the ALD process such as methyl groups or other organics. To address this, we annealed the coated aerogel sample at 700°C for 24 hrs and recharacterized the aerogel. The annealed coated aerogel only increased its thermal losses by 10%, which is still less than half of an uncoated control sample. This demonstrates that the interfacial layer is responsible for the increased infrared absorption. We also attribute the decrease in heat flux to the increased infrared absorption because conduction is a minimal factor in vacuum and at high temperatures.

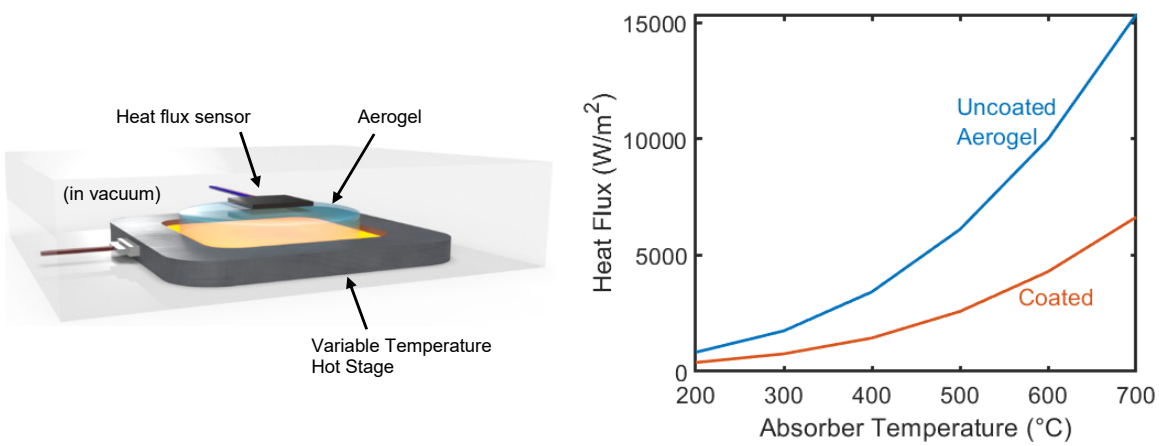


**Figure 17. Measured heat losses at various absorber surface temperatures from the ALD-coated aerogels.**

## 6.2 Thermal stability of ALD-coated aerogels

In partial fulfillment of EOP-B.

| | | | | | | |
|---|---|---|---|---|---|---|
| EOP-B | 18 | Receiver efficiency (rel.) degradation: cumulative, terminal rate | < 0.25%/10 hrs rate (70-100 hrs).<br><br>constraint: 700C | **Student t-test.** RTE-HTE efficiency prediction based on solar transmittance, thermal conductivity, and infrared absorption. At least 5 measurements taken on each sample after each anneal (Average, 90% CI). At least 3 aerogels measured. | Data and report sent to DOE for verification. Data format: solar transmittance (%), thermal conductivity (W/mK), infrared absorption (1/cm), and modeled receiver efficiency (%) as a function of annealing time. | 0.25% is within the range of uncertainty of our characterization tools. |

We annealed aerogels for up to 96 hours at 700°C (Figure 18). The results from two of each uncoated and coated aerogels show that coated aerogels have much greater thermal stability compared to uncoated aerogels. Compared to the initial area of each, the coated aerogel decreases by 15.3% compared to 30.1% for the uncoated aerogels. Furthermore, the coated aerogels demonstrate long term stability as the area only decreased 0.0310% for every 10 hours from 48 to 96 hours. On the other hand, the uncoated aerogels are unstable at such conditions and shrink at a rate 10x faster (0.38%/10 hours).

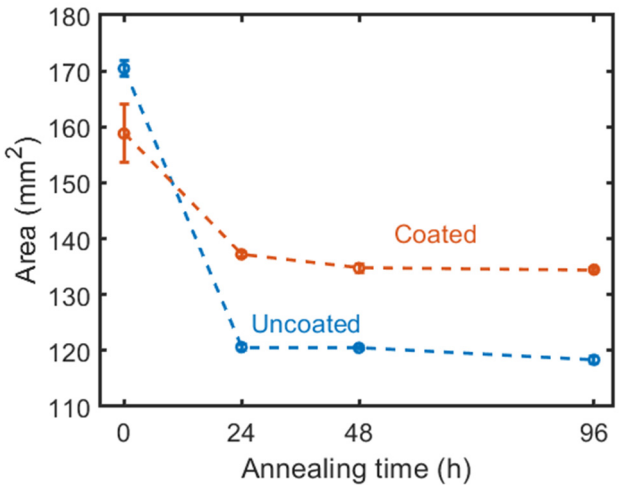


**Figure 18. Thermal stability of aerogels at 700ºC in air. Area refers to footprint of aerogel.**

The primary driving force for shrinkage/densification of aerogels at elevated temperatures is minimization of surface energy. The kinetics of surface diffusion are activated by elevated temperatures. The role of alumina, we suspect, is to stabilize the surface atoms and slow down the kinetics. The uniformity and quality of the coating is particularly important in this regard because defects and grain boundaries can facilitate surface diffusion and ultimately unwanted densification.

## 7. Modeling efficiency and cost of a line-focusing system with aerogels

In partial fulfillment of EOP-C.

| | | | | | | |
|---|---|---|---|---|---|---|
| EOP-C | 18 | Modeled efficiency and cost in a realistic CSP configuration | >60% collector efficiency at 700C (optical x receiver); LCOE below SOA | **Student t-test. 95% Confidence Interval.** PTC/LFR and cost models compared against literature/DOE benchmarks. Models used to predict efficiency and cost of aerogel-based PTC/LFR collectors. | Model and report sent to DOE for verification. Model format: Excel. Data format: LCOE ($/kWh), efficiency (%) (vs. temperature, concentration) | Value was chosen to be competitive with central receivers (>90% receiver eff., 55% optical eff.). |

## 7.1 Linear receiver heat transfer model

To model the performance of a linear receiver, we modified a simple heat transfer model used in a 2009 NREL report on heat loss testing for a linear receiver.[51] The modifications were made to reflect the design of the SunTrap receiver (Norwich).[52] We used the design specifications (e.g. diameter, conductivities of insulation and glass) in our calculations. The SunTrap design insulates the non-incident regions of a cylindrical receiver, while using an air cavity to insulate the incident surface. The modified model treats conductive and radiative losses in parallel. Specifically, for conductive/convective losses, we used a resistance network shown in Figure 19.

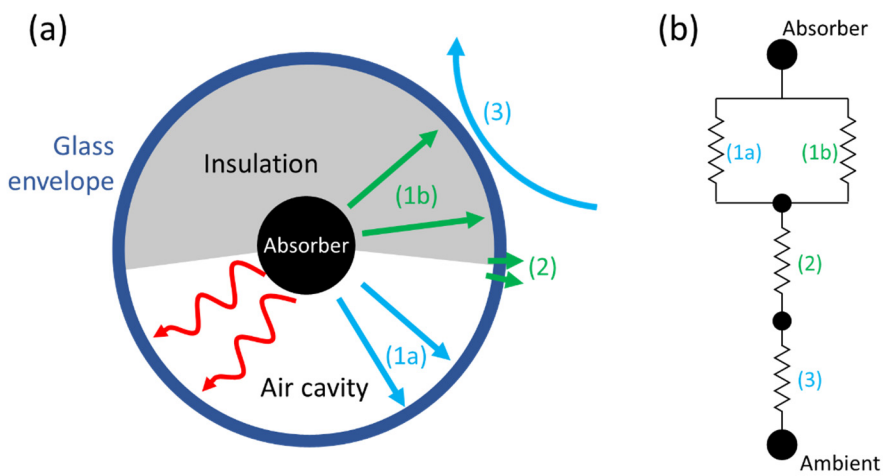


**Figure 19. Linear receiver heat transfer model. (a) Diagram of the heat transfer pathways. Blue arrows indicate convection, green arrows indicate conduction, and red arrows indicate radiation. (b) Resistance diagram of the conductive/convective pathway.**

Convection through the air cavity was modeled by determining the Grashof, Prantl, and Rayleigh numbers of the air in the cavity. An empirical model was then used to compute the effective thermal conductivity of the air. We used a thermal conductivity of 0.033 W/m/K for the insulation, a thermal conductivity of 1.1 W/m/K for the glass, and an external convective heat transfer coefficient of 5 W/m$^2$/K. At 700°C, we used absorber emissivities of 0.25 and 0.13 for the selective surface and coated aerogel, respectively. We chose 0.25 because that is the lowest emissivity for selective surfaces to date for measurements over 700°C. As for the solar absorptance, we assumed a value of 0.95 for the selective surface. For the coated aerogel, we used the solar-weighted transparency (0.92) because we assume they will be paired with near-blackbody absorbers. Lastly, when we modeled the heat transfer for the coated aerogel, we included another conductive resistive pathway for conduction through the aerogel. We used a thermal conductivity of 0.033 W/m/K for the aerogel.

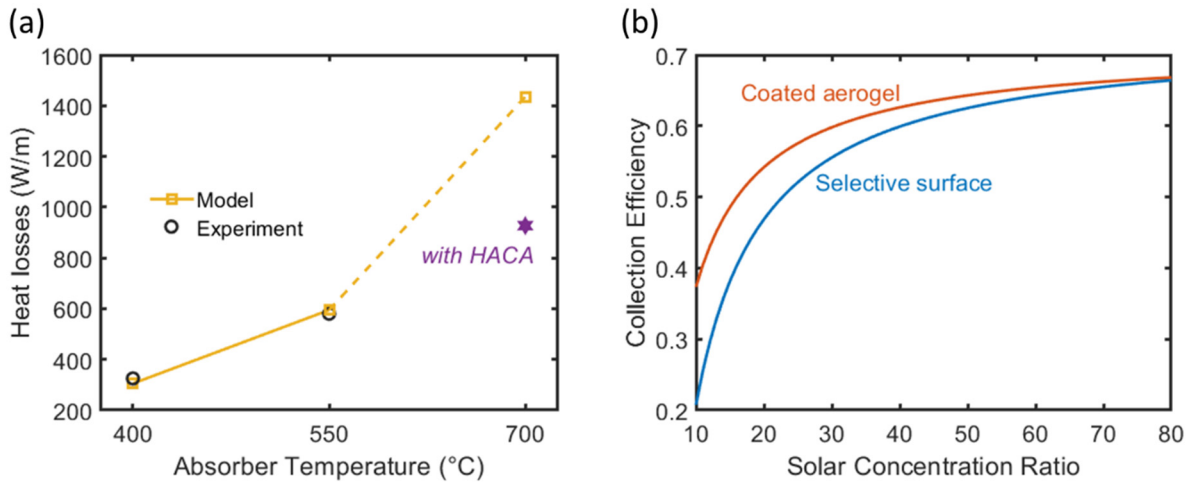


**Figure 20. Heat losses and collection efficiency from linear receiver model. (a) Validation of the linear receiver heat loss model. The loss model agrees well with experimental data[52]. (b) Collection efficiency (product of optical and receiver) vs. solar concentration ratio for selective surfaces and coated aerogels. The coated aerogel outperforms the selective surface due to its ability to suppress heat losses.**

We first validated the model by comparing our results to experimental results in a 2019 report on the SunTrap receiver.[52] Our modeled results agree well with the experimental ones. Our model shows that the coated aerogel suppresses heat losses at high temperatures compared to selective surfaces (Figure 20a). This significant reduction in heat losses enables higher receiver efficiencies at low optical concentrations (Figure 20b).

## 7.2 Cost modeling using SAM

We used the System Advisor Model (SAM), developed by NREL, to estimate the effect that using aerogels has on LCOE of line-focusing systems. A 100 MWe plant with a field size of 900,000 $m^2$ was chosen for Tuczon, AZ. For all the models, all variables were kept unchanged except for the operating temperatures, cycle efficiencies, and receiver performance. Option 2 was used (defining field aperture size) over solar multiple because it kept the size of the plant more consistent as the receiver losses define the field size for a constant solar multiple.

To model a supercritical $CO_2$ ($sCO_2$) cycle in the parabolic trough design, we first computed the cycle parameters in a solar power tower design. We defined the cycle efficiency and inlet temperature, and SAM computed the outlet temperature (Table 1). The efficiencies for each temperature were pulled from literature[2].

**Table 4. Inputs and results from $sCO_2$ cycle analysis.**

| Turbine Inlet Temperature | Turbine Outlet Temperature (°C) | Cycle Efficiency |
|---|---|---|
| 550 | 406.72 | 0.44 |
| 600 | 448 | 0.46 |

| | | |
|---|---|---|
| 650 | 491 | 0.48 |
| 700 | 535 | 0.5 |

We adjusted the temperature-dependent solar absorptance and thermal emittance values for the solar receivers. The temperature-dependent emittance of selective surfaces was pulled from literature[45] as it one of the few publications with reported temperature-dependent emittances up to 700°C. Although, it should be noted that this selective surface was not stable above 600°C. [45] For the solar absorptance, we used values of 0.95[45] and 0.93 for the selective surface and coated aerogel, respectively. The temperature-dependent emittances are provided in Table 2. The effective emittance for the coated aerogels is calculated from the experimental heat loss measurements.

**Table 5. Emittance values for selective surfaces and the coated aerogel.**

| Temperature (°C) | Selective Surface[45] | Coated Aerogel |
|---|---|---|
| 300 | 0.097 | 0.1236 |
| 400 | 0.121 | 0.1234 |
| 500 | 0.150 | 0.1273 |
| 600 | 0.185 | 0.1302 |
| 700 | 0.224 | 0.1304 |

The increased receiver efficiency from using the coated aerogel's effective emittance results in a lower LCOE for operating temperatures above 650°C. Note that for 700°C, the SAM is incapable of producing results for the given conditions. Most of the outputs from the model say "Inf."

**Table 6. LCOE and capacity factor comparing aerogel to SOA**

| Temperature (°C) | Selective Surfaces | | Coated Aerogel | |
|---|---|---|---|---|
| | LCOE | Capacity factor | LCOE | Capacity factor |
| 391 (Default Steam) | 11.67 | 40.0 | 12.20 | 38.2 |
| 550 | 11.52 | 37.3 | 11.78 | 36.5 |
| 600 | 12.60 | 33.7 | 13.08 | 32.5 |
| 650 | 17.31 | 24.2 | 13.85 | 30.4 |
| 700 | N/A | N/A | N/A | N/A |

The results here show that the coated aerogels enable more efficient lower operating costs for temperatures necessary next-gen CSP. Future SAM modeling will need to correct to reflect more accurately the cost savings of switching more accurately to a $sCO_2$ power cycle.

## Significant Accomplishments and Conclusions:

We have achieved the following major technical milestones:

- Predicted receiver efficiency – Parametric regions with 80% efficiency (PROPS80) have been identified that serve as a guide for design of solar-transparent insulating materials (TIMs).
- Heat loss measurement accuracy and temperature range – Measurement setup has been assembled and is functioning as expected. We have demonstrated the accuracy of the measurement technique and its temperature range.
- Uniform concentration of ALD coating – By optimizing the duration of each ALD step, we are able to uniformly coat aerogels. It is possible to predict the process parameters required for complete coating based on an analytical model that is consistent with our experimental characterization of penetration depth.
- RTE model validation – We have implemented models to capture the infrared properties and predict scattering of multi-component aerogels. Models have been experimentally validated.
- Solar (AM1.5D) transmittance, thermal conductivity, infrared absorption coefficient – ALD-coated samples meeting PROPS80 criteria have been fabricated.

Our best uncoated silica aerogels achieved a solar weighted transmittance of over 96%. Our most transparent multicomponent (ALD coated) aerogel to date achieved a solar weighted transparency of 92.2 ± 0.01%. Despite the ~4% decrease in solar transparency, the multicomponent aerogels show significantly higher infrared absorption, even after annealing at 700°C. Unlike uncoated silica aerogels, which become more transparent in the infrared after annealing at high temperatures, our multicomponent aerogels demonstrate high infrared absorption after annealing at 700ºC. The alumina coating increases the infrared absorption broadly across the region from 2 - 5 microns. This is important since this is where most radiative losses occur in silica aerogels. Meanwhile, the thermal conductivity of the aerogels exhibited a small change due to the ALD coating, consistent with the mass increase resulting from the coating.

The figure below summarizes the relevant properties of our ALD-coated aerogels and compares them to the properties of the state-of-the-art (SoA) aerogels published in literature. Based on the three important material properties, our aerogels are capable of surpassing 80% efficiency at 700 C and 100 Suns. Furthermore, our thermal aging study shows that that coated aerogels have much greater thermal stability compared to silica aerogels.

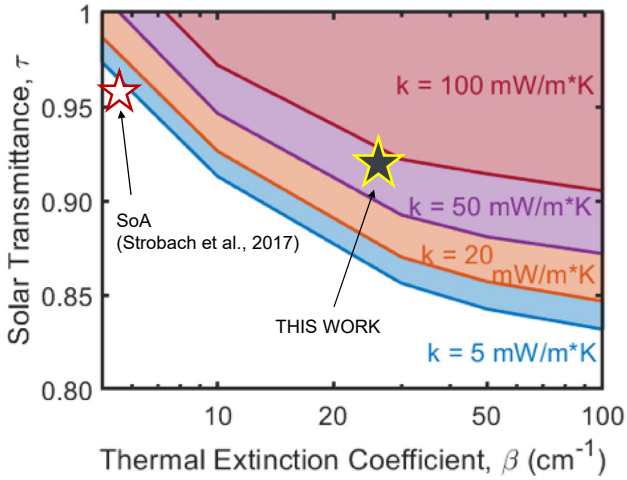


**Figure 21. Properties of our ALD-coated aerogels (this work) relative to best reported aerogels in literature**

## Inventions, Patents, Publications, and Other Results:

### Patents

Andrej Lenert; Neil Dasgupta; Zachary Berquist; Andrew Gayle. Transparent Mesoporous Materials and Devices Comprising the Same. Provisional patent filed. 30275/55692/US.

### Publications

Zachary Berquist, Kevin Turaczy, and Andrej Lenert Plasmon-Enhanced Greenhouse Selectivity for High Temperature Solar Thermal Energy Conversion. *ACS Nano*. 2020 https://doi.org/10.1021/acsnano.0c04982. **OSTI# 1673748**

### Conference Presentations

Zachary Berquist, Ashley R. Beilinski, Andrew Gayle, Hannah Kim, Neil P. Dasgupta, and Andrej Lenert. Plasmon-Enhanced Selective Radiative Transmission in Aerogels. HT2019-3462. Nanoscale Thermal Radiation / K-9 / 2019 Summer Heat Transfer Conference. Bellevue, WA. 07/15/19

Zachary Berquist, Ashley R. Beilinski, Andrew Gayle, Hannah Kim, Neil P. Dasgupta, and Andrej Lenert. Plasmonic Multicomponent Aerogels for Solar Thermal Energy Conversion. DD03 Thermoelectrics and Thermal Transport / Electronic Materials Conference. Ann Arbor, MI. 06/27/19.

Zachary Berquist, Andrew Gayle, Neil P. Dasgupta, and Andrej Lenert. Investigating the Thermal Stability of Silica Aerogels at Gen3 CSP Temperatures. 14th International Conference on Energy Sustainability. Virtual 06/17/20.

Zachary Berquist, Kevin Turaczy, and Andrej Lenert Infrared Plasmonic Oxides for Selectively Transparent Aerogels in High Temperature Solar Receivers. 62nd Electronic Materials Conference. Virtual 06/25/20.

**Awards**

Andrej Lenert. 3M Foundation Non-Tenured Faculty Award. 2020.

Zachary Berquist. First Place Presentation at 14th ES Conference. 06/17/20.

**Press**

$1.6M funds solar cell windows, high-temperature solar power. The University Record. https://record.umich.edu/articles/16m-funds-solar-cell-windows-high-temperature-solar-power

## Path Forward:

Our SIPS project focused on co-optimization of aerogel microstructure and ALD process parameters to achieve receiver efficiencies above 80% (at 700°C and 100 Suns), as well as de-risking of important material characteristics and processing approaches. Specifically, the ability to conformally coat the aerogel with ALD-grown refractory oxides has produced favorable material properties, as evaluated through long-duration thermal stability tests and temperature-dependent heat loss measurements. Furthermore, the heat loss measurements validate our heat transfer models and efficiency predictions. These models can be used to design and optimize a practical receiver configuration that is paired with a linear Fresnel or parabolic trough concentrator. The project has also uncovered a gap in CSP system-level modeling tools (e.g., SAM) when it comes to line-focusing collectors paired with high-temperature $sCO_2$ cycles that needs to be addressed in order to provide a more accurate estimate of LCOE.

Funding is now crucial for co-optimization of the receiver enclosure and aerogel design, scale up of materials and processes, and high-temperature receiver testing. The immediate next goal should be to demonstrate synthesis and ALD at a wafer scale (6-12 inch) without significant loss of key properties. Once scaled-up, a prototype receiver should be built and tested at temperature to evaluate heat losses and validate models. The stability of the aerogels under simulated diurnal thermal cycling within this prototype receiver should be characterized. If the aerogel technology continues to show promise at this stage, it should proceed to testing in an operational environment (TRL 6: on-sun, high temperature, diurnal cycling) at a solar test facility.

## References:


1. US Department of Energy. Solar Research Spotlight: Concentrating Solar Thermal Power. *Off. Energy Effic. Renew. Energy* (2018).
2. Turchi, C. S., Ma, Z., Neises, T. W. & Wagner, M. J. Thermodynamic study of advanced supercritical carbon dioxide power cycles for concentrating solar power systems. *J. Sol. Energy Eng. Trans. ASME* **135**, (2013).
3. Vannoni, C., Battisti, R. & Drigo, S. *Potential for Solar Heat in Industrial Processes*. (2008).
4. *Monthly Energy Review March 2020*. (Energy Information Agency, 2020).
5. *Roadmap for Process Heating Technology Roadmap for Process Heating*. (Industrial Heating Equipment Assoication and U.S. Department of Energy, 2001).
6. *AEO2020 Transportation*. *Annual Energy Outlook* (Energy Information Agency, 2020).
7. Mehos, M. *et al. Concentrating Solar Power Gen3 Demonstration Roadmap*. *NREL* (2017).
8. Selvakumar, N. & Barshilia, H. C. Review of physical vapor deposited (PVD) spectrally selective coatings for mid- and high-temperature solar thermal applications. *Sol. Energy Mater. Sol. Cells* **98**, 1–23 (2012).
9. Li, P. *et al.* Large-Scale Nanophotonic Solar Selective Absorbers for High-Efficiency Solar Thermal Energy Conversion. *Adv. Mater.* **27**, 4585–4591 (2015).
10. Zhou, L. *et al.* Self-assembled spectrum selective plasmonic absorbers with tunable bandwidth for solar energy conversion. *Nano Energy* **32**, 195–200 (2017).
11. Kondaiah, P., Niranjan, K., John, S. & Barshilia, H. C. Tantalum carbide based spectrally selective coatings for solar thermal absorber applications. *Sol. Energy Mater. Sol. Cells* **198**, 26–34 (2019).
12. Xu, K. *et al.* A review of high-temperature selective absorbing coatings for solar thermal applications. *J. Mater.* **6**, 167–182 (2020).
13. Kittel, C. *Introduction to Solid State Physics*. (John Wiley & Sons, Inc., 1967).
14. Doiron, C. F. & Naik, G. V. Semiconductors for high selectivity thermal emitters. *J. Opt.* **20**, (2018).
15. Yeng, Y. X. *et al.* Enabling high-temperature nanophotonics for energy applications. *Proc. Natl. Acad. Sci. U. S. A.* **109**, 2280–2285 (2012).
16. Burger, T., Sempere, C. & Lenert, A. Thermophotovoltaic energy conversion: materials and device engineering. *Nanoscale Energy Transport* (2020) doi:10.1088/978-0-7503-1738-2ch17.

17. Cao, F. *et al.* A high-performance spectrally-selective solar absorber based on a yttria-stabilized zirconia cermet with high-temperature stability. *Energy Environ. Sci.* **8**, 3040–3048 (2015).

18. Kraemer, D., McEnaney, K., Cao, F., Ren, Z. & Chen, G. Accurate determination of the total hemispherical emittance and solar absorptance of opaque surfaces at elevated temperatures. *Sol. Energy Mater. Sol. Cells* **132**, 640–649 (2015).

19. Zhang, K. *et al.* A review on thermal stability and high temperature induced ageing mechanisms of solar absorber coatings. *Renew. Sustain. Energy Rev.* **67**, 1282–1299 (2017).

20. Barlev, D., Vidu, R. & Stroeve, P. Innovation in concentrated solar power. *Sol. Energy Mater. Sol. Cells* **95**, 2703–2725 (2011).

21. Wei, X. *et al.* A new method for the design of the heliostat field layout for solar tower power plant. *Renew. Energy* **35**, 1970–1975 (2010).

22. Tzivanidis, C., Bellos, E., Korres, D., Antonopoulos, K. A. & Mitsopoulos, G. Thermal and optical efficiency investigation of a parabolic trough collector. *Case Stud. Therm. Eng.* **6**, 226–237 (2015).

23. Kaushika, N. D. & Sumathy, K. Solar transparent insulation materials: A review. *Renew. Sustain. Energy Rev.* **7**, 317–351 (2003).

24. Weinstein, L. A. *et al.* A Hybrid Electric and Thermal Solar Receiver. *Joule* **2**, 962–975 (2018).

25. Rubin, M. & Lampert, C. M. Transparent silica aerogels for window insulation. *Sol. Energy Mater.* **7**, 393–400 (1983).

26. Caps, R. & Fricke, J. Infrared Radiative Heat Transfer in Highly Transparent Silica Aerogel. *Sol. Energy* **36**, 361–364 (1986).

27. McEnaney, K., Weinstein, L., Kraemer, D., Ghasemi, H. & Chen, G. Aerogel-based solar thermal receivers. *Nano Energy* **40**, 180–186 (2017).

28. Kashyap, V. *et al.* Full Spectrum Solar Thermal Energy Harvesting and Storage by a Molecular and Phase-Change Hybrid Material. *Joule* **3**, 3100–3111 (2019).

29. Strobach, E., Bhatia, B., Yang, S., Zhao, L. & Wang, E. N. High temperature annealing for structural optimization of silica aerogels in solar thermal applications. *J. Non. Cryst. Solids* **462**, 72–77 (2017).

30. Lenza, R. F. S. & Vasconcelos, W. L. *Preparation of Silica by Sol-Gel Method Using Formamide*. (2001).

31. Zhao, L. *et al.* Harnessing Heat beyond 200 °c from Unconcentrated Sunlight with Nonevacuated Transparent Aerogels. *ACS Nano* **13**, 7508–7516 (2019).

32. Gunay, A. A. *et al.* Optically Transparent – Thermally Insulating Silica Aerogels for

Solar Thermal Insulation. *ACS Appl. Mater. Interfaces* **10**, 12603–12611 (2018).

33. Tillotson, T. M. & Hrubesh, L. W. Transparent ultralow-density silica aerogels prepared by a two-step sol-gel process. *J. Non. Cryst. Solids* **145**, 44–50 (1992).

34. Shafi, S., Navik, R., Ding, X. & Zhao, Y. Improved heat insulation and mechanical properties of silica aerogel/glass fiber composite by impregnating silica gel. *J. Non. Cryst. Solids* **503**–**504**, 78–83 (2019).

35. Kwon, Y., Choi, S., Kang, E.-S. & Baek, S.-S. Ambient-dried silica aerogel doped with TiO2 powder for thermal insulation. *J. Mater. Sci.* **35**, 6075–6079 (2000).

36. Kuhn, J., Gleissner, T., Arduini-Schuster, M. C., Korder, S. & Fricke, J. Integration of mineral powders into SiO2 aerogels. *J. Non. Cryst. Solids* **186**, 291–295 (1995).

37. Lee, D., Stevens, P. C., Zeng, S. Q. & Hunt, A. J. Thermal characterization of carbon-opacified silica aerogels. *J. Non. Cryst. Solids* **186**, 285–290 (1995).

38. Strobach, E., Bhatia, B., Yang, S., Zhao, L. & Wang, E. N. High temperature stability of transparent silica aerogels for solar thermal applications. *APL Mater.* (2019) doi:10.1063/1.5109433.

39. Rinnerbauer, V. *et al.* Metallic photonic crystal absorber-emitter for efficient spectral control in high-temperature solar thermophotovoltaics. *Adv. Energy Mater.* **4**, (2014).

40. Biener, M. M. *et al.* ALD functionalized nanoporous gold: Thermal stability, mechanical properties, and catalytic activity. *Nano Lett.* (2011) doi:10.1021/nl200993g.

41. Beck, A., Caps, R. & Fricke, J. Scattering of visible light from silica aerogels. *J. Phys. D. Appl. Phys.* (1989) doi:10.1088/0022-3727/22/6/002.

42. Heinemann, U., Caps, R. & Fricke, J. Radiation-conduction interaction : An investigation on silica aerogels. *Int. J. Heat Mass Transf.* **39**, 2115–2130 (1996).

43. Zheng, Q., Kaur, S., Dames, C. & Prasher, R. S. Analysis and improvement of the hot disk transient plane source method for low thermal conductivity materials. *Int. J. Heat Mass Transf.* **151**, (2020).

44. Berquist, Z. J., Turaczy, K. K. & Lenert, A. Plasmon-Enhanced Greenhouse Selectivity for High-Temperature Solar Thermal Energy Conversion. *ACS Nano* (2020) doi:10.1021/acsnano.0c04982.

45. Wang, H., Alshehri, H., Su, H. & Wang, L. Design, fabrication and optical characterizations of large-area lithography-free ultrathin multilayer selective solar coatings with excellent thermal stability in air. *Sol. Energy Mater. Sol. Cells* **174**, 445–452 (2018).

46. Garín, M., Hernández, D., Trifonov, T. & Alcubilla, R. Three-dimensional metallo-dielectric selective thermal emitters with high-temperature stability for

thermophotovoltaic applications. *Sol. Energy Mater. Sol. Cells* **134**, 22–28 (2015).

47. Zhou, Z. *et al.* High-temperature, spectrally-selective, scalable, and flexible thin-film Si absorber and emitter. *Opt. Mater. Express* **10**, 208 (2020).

48. Aksay, I. A., Dabbs, D. M. & Sarikaya, M. Mullite for Structural, Electronic, and Optical Applications. *J. Am. Ceram. Soc.* **74**, 2343–2358 (1991).

49. Shinohara, N., Dabbs, D. M. & Aksay, I. A. Infrared Transparent Mullite Through Densification Of Monolithic Gels At 1250°C. *Infrared Opt. Transm. Mater.* **0683**, 19 (1986).

50. Stoch, J., Lercher, J. & Ceckiewicz, S. Correlations between XPS binding energies and composition of aluminasilicate and phosphate molecular sieves. *Zeolites* **12**, 81–85 (1992).

51. Burkholder, F. & Kutscher, C. F. Heat loss testing of Schott's 2008 PTR70 parabolic trough receiver. *NREL Tech. Rep.* 58 (2009).

52. Stettenheim, J., McBride, T., Brambles, O. & Johnson, L. *Field Testing of Manufacturable Advanced Low-Cost Receiver for Parabolic Trough Solar Power*. (2019) doi:10.1109/GreenTech.2019.8767118.